

Multiscale Architected Membranes, Electrodes, and Transport Layers for Next-Generation Polymer Electrolyte Membrane Fuel Cells

Segeun Jang, Yun Sik Kang, Dohoon Kim, Subin Park, Changwook Seol, Sungchul Lee,* Sang Moon Kim,* and Sung Jong Yoo*

Over the past few decades, considerable advances have been achieved in polymer electrolyte membrane fuel cells (PEMFCs) based on the development of material technology. Recently, an emerging multiscale architecting technology covering nanometer, micrometer, and millimeter scales has been regarded as an alternative strategy to overcome the hindrance to achieving high-performance and reliable PEMFCs. This review summarizes the recent progress in the key components of PEMFCs based on a novel architecture strategy. In the first section, diverse architectural methods for patterning the membrane surface with random, single-scale, and multiscale structures as well as their efficacy for improving catalyst utilization, charge transport, and water management are discussed. In the subsequent section, the electrode structures designed with 1D and 3D multiscale structures to enable low Pt usage, improve oxygen transport, and achieve high electrode durability are elucidated. Finally, recent advances in the architected transport layer for improving mass transportation including pore gradient, perforation, and patterned wettability for gas diffusion layer and 3D structured/engineered flow fields are described.


1. Introduction

As the effort to shift from a carbon emission economy to a renewable carbon-free future intensifies, polymer electrolyte membrane fuel cells (PEMFCs) have received considerable attention worldwide. This is because of the excellent energy conversion efficiency, low operating temperature, and zero harmful pollutant emission of PEMFCs.^[1,2] Over the decades, significant advances in key fuel cell components have enabled the partial commercialization of PEMFCs as a green power source in several commercial energy markets. The markets include those of fuel cell electric vehicles, forklifts, unmanned aerial vehicles, and power generators for buildings.^[3–8] However, certain technical problems, such as the high cost of precious metal catalysts, limited fuel

S. Jang, D. Kim
School of Mechanical Engineering
Kookmin University
Seoul 02707, Republic of Korea

Y. S. Kang
Fuel Cell Laboratory
Korea Institute of Energy Research (KIER)
Daejeon 34129, Republic of Korea

S. Park, S. J. Yoo
Hydrogen and Fuel Cell Research
Korea Institute of Science and Technology (KIST)
Seoul 02792, Republic of Korea
E-mail: ysj@kist.re.kr

 The ORCID identification number(s) for the author(s) of this article can be found under <https://doi.org/10.1002/adma.202204902>.

© 2023 The Authors. Advanced Materials published by Wiley-VCH GmbH. This is an open access article under the terms of the Creative Commons Attribution-NonCommercial-NoDerivs License, which permits use and distribution in any medium, provided the original work is properly cited, the use is non-commercial and no modifications or adaptations are made.

DOI: 10.1002/adma.202204902

C. Seol, S. M. Kim
Department of Mechanical Engineering
Incheon National University
Incheon 22012, Republic of Korea
E-mail: ksm7852@inu.ac.kr

S. Lee
Fuel Cell Core Parts Development Cell
Hyundai Mobis Co. Ltd.
Uiwang 16082, Republic of Korea
E-mail: scata@mobis.co.kr

S. J. Yoo
KHU-KIST Department of Converging Science and Technology
Kyung Hee University
26, Kyungheedaero, Dongdaemun-gu, Seoul 02447, Republic of Korea

S. J. Yoo
Division of Energy & Environment Technology
KIST School
University of Science and Technology (UST)
Daejeon 34113, Republic of Korea

cell performance due to sluggish oxygen reduction reaction (ORR) kinetics, and Ohmic and mass transport losses, retard the economic viability of PEMFCs in markets. The foregoing is attributed to the unoptimized PEMFC components—catalyst, electrolyte membrane, electrode, and transport layers and their interfaces. These components perform a critical role in generating electricity (through electrochemical reactions) and transporting reactant gases, ions, and water.^[9–13]

To address these issues, considerable efforts have been devoted to developing low-cost, reliable, stable, and high-performance electrocatalysts, membrane electrode assemblies (MEAs), and transport layers.^[14–16] In the early development stage of PEMFCs, material-oriented research on each component had mainly been conducted. In the case of the membrane, perfluorinated sulfonic acid (PFSA)-based membranes, such as Nafion membranes, have been widely used in PEMFCs because of their high proton conductivity and high mechanical and chemical stability.^[17] However, the Nafion membranes still have limitations regarding relatively high fuel crossover, low glass transition temperature, high manufacturing cost, and environmental issues due to the fluorination process.^[18] Therefore, there have been extensive studies for developing reinforced PFSA-based composite membranes^[19–21] as well as non-PFSA-based membranes such as low-cost hydrocarbon-based electrolytes.^[22,23] Recently, research employing an architecturing strategy has emerged in line with the development of various synthesis methods as well as micro- and nano-patterning techniques. Membrane surface engineering approaches via diverse patterning processes have been introduced because a flat commercial Nafion membrane has limitations in maximizing the catalyst utilization and active sites for reaction at the interface between the membrane surface and electrode. The PEMFC performance is enhanced when a patterned membrane is incorporated into the MEA. For example, the increase in electrochemical active surface area (ECSA) due to enlarged membrane/electrode interface, reduction in Ohmic resistance by membrane thinning, and improvement in water removal capacity from a structural effect have been reported.^[20,24,25] When it comes to an electrode (catalyst layer), advanced Pt alloy catalysts with high durability (such as nanowhiskers, core-shell catalysts, intermetallic catalysts, surface-controlled catalysts, supportless catalysts, and single-atom catalysts) and ORR activity have been developed.^[26–28] Together with the foregoing, the structural engineering of the electrode (consisting of ionomer, catalysts, and pores) has been actively implemented in terms of MEA performance and stability. Most studies have focused on controlling the pore size distribution and changing the morphological configuration of conventional 2D flat electrode to have a 1D or 3D multiscale structure. The foregoing can facilitate mass transport, improve durability, and enable the effective use of noble metal catalysts.^[29–31] Furthermore, optimizing the structural design of the gas diffusion layer (GDL) and flow channel in bipolar plates has been explored. The goal is to improve the water management and reactant distribution in the electrode by imposing patterned wettability for separating water and gas passages, applying pore gradient (PG), and constructing 3D and multiscale structures.^[32–35]

As briefly mentioned above, the architecturing strategy in PEMFCs along with material development has recently been

the main focus of attention. However, published articles dealing with these architectural approaches for developing PEMFCs are few compared with the numerous articles on the development of electrolyte membranes or catalysts. The current presumption is that the architecturing strategy can be a breakthrough in attaining a high-performance and reliable fuel cell technology that is highly compatible with the developed and existing materials used in PEMFCs. Accordingly, this review focuses on a comprehensive multiscale architecturing strategy for high-performance PEMFCs. It covers the structural designs and modifications of the electrolyte membrane, electrodes, GDL, and bipolar plates. The review also considers the effect of the foregoing on the PEMFC performance by investigating the changes in catalytic, Ohmic, and mass transport properties (**Figure 1**).

Because the performance of a PEMFC is determined by three main overpotentials, checking the governing equation for each overpotential to ascertain how the morphological and structural factors of the component affect device performance is necessary. The governing equation for the operating cell voltage is expressed as follows:^[2,39]

$$E_{\text{cell}} = E_{\text{rev}} - \eta_{\text{kinetic}} - \eta_{\text{ohmic}} - \eta_{\text{mass}} \quad (1)$$

where E_{cell} is the operating cell voltage, E_{rev} is the reversible voltage, η_{kinetic} is the kinetic overpotential, η_{ohmic} is the Ohmic overpotential, and η_{mass} is the mass-transport (concentration) overpotential. The kinetic overpotential, η_{kinetic} , can be expressed as a function of L_c .^[40,41]

$$\eta_{\text{kinetic}} = \left(\frac{RT}{\alpha n F} \right) \ln \frac{j}{j_0} = \left(\frac{RT}{\alpha n F} \right) \ln \frac{j}{L_c j_0} \quad (2)$$

where R is the gas constant, T is the operational temperature, α is the transfer coefficient, n is the number of electrons participating in the electrochemical reaction, F is Faraday's constant, j is the current density during operation, j_0 is the exchange current density (A cm^{-2}), j_0 is the catalyst-specific exchange current density (A g^{-1}), and L_c is the effective catalyst loading per unit area (g cm^{-2}). In this equation, high values of j_0 and α indicate that the reaction can be easily initiated by decreasing η_{kinetic} . These parameters are directly related to how well the catalyst is designed to achieve a high ORR. Moreover, note that η_{kinetic} is inversely proportional to L_c , depending on the absolute catalyst loading amount and the morphological characteristics of electrode structures directly affecting the ECSA. Therefore, increasing the ECSA through the proper design of the membrane/electrode interface and electrode structure is critical for improving the PEMFC performance while minimizing the usage of precious metal catalysts.

The Ohmic overpotential, η_{ohmic} , comprises the proton transport resistance through the membrane (R_{mem}) and the ionomer network of the electrode ($R_{\text{H}^+, \text{CL}}$), and the overall electrical resistance of the system (R_{elec}):

$$\eta_{\text{ohmic}} = j R_{\text{ohmic}} = j (R_{\text{mem}} + R_{\text{H}^+, \text{CL}} + R_{\text{elec}}) \quad (3)$$

To ensure high proton transport through the membrane, developing a high-ion conductive membrane and reducing the membrane thickness are necessary for reducing R_{mem} . In

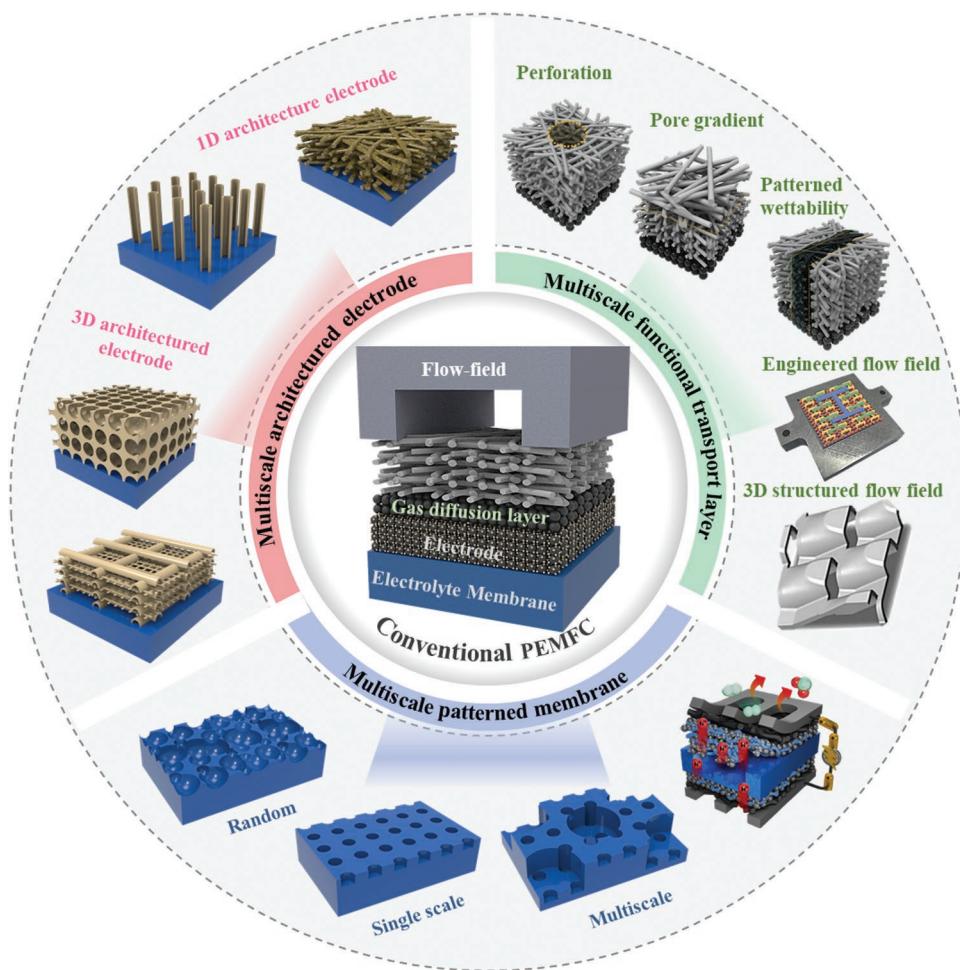


Figure 1. Overview of multiscale architected membrane, electrodes, and transport layer for high-performance PEMFCs. Engineered flow field: Reproduced with permission.^[36] Copyright 2018, Royal Society of Chemistry. 3D structured flow field: Reproduced with permission.^[37] Copyright 2019, Elsevier. Multiscale membrane: Reproduced with permission.^[38] Copyright 2015, Springer Nature.

addition, it is required to increase the proton conductivity by optimizing the electrode structure and composition as well as the membrane/electrode interface for reducing $R_{H^+,CL}$.

Finally, the mass transport overpotential, η_{mass} , is expressed as^[2,42]

$$\eta_{mass} = \frac{RT}{nF} \ln \left(\frac{C_{O_2}}{C_{O_2}^0} \right) = \frac{RT}{nF} \left(1 + \frac{1}{\alpha} \right) \ln \left(\frac{j_L}{j_L - j} \right) \quad (4)$$

where C_{O_2} is the local concentration of oxygen gas in the electrode, and $C_{O_2}^0$ is the bulk concentration of oxygen gas in the flow channel. This equation (including the geometrical factors, i.e., porosity and thickness of the transport layer and electrode) can be rewritten as^[2]

$$j_L = nFD^{\text{eff}} \frac{C_{O_2}^0}{\delta}, D^{\text{eff}} = \varepsilon^k D (k: \text{constant}) \quad (5)$$

where j_L is the limiting current density, ε is the porosity of the electrode, D is the nominal diffusivity of the product, D^{eff} is the effective diffusivity of the product, and δ is the thickness of the transport layer and electrode. The equation indicates that

η_{mass} is proportional to δ and inversely proportional to the bulk concentration of the reactants ($C_{O_2}^0$) in the flow channel and the porosity of the transport layer and electrode (ε). This implies that a proper structural design (including an electrode, a GDL, and a bipolar flow channel) is highly necessary to improve the mass transport by reducing δ while securing high ε value and $C_{O_2}^0$ concentration. Additionally, effective water management is crucial because the water generated by the ORR facilely fills the pores of the electrode and covers the catalyst surface. This severely restricts the transport of reactant gas to the electrochemically active sites in the electrode. To resolve the mass transport problem due to ineffective water management, the construction of well-designed structures based on an architecturing strategy is necessary to remove the generated water effectively.

2. Surface Modification of Membrane

A key component for determining the cost, durability, and performance of fuel cells is MEA, which consists of an electrolyte membrane sandwiched between the anode and cathode.^[43] In

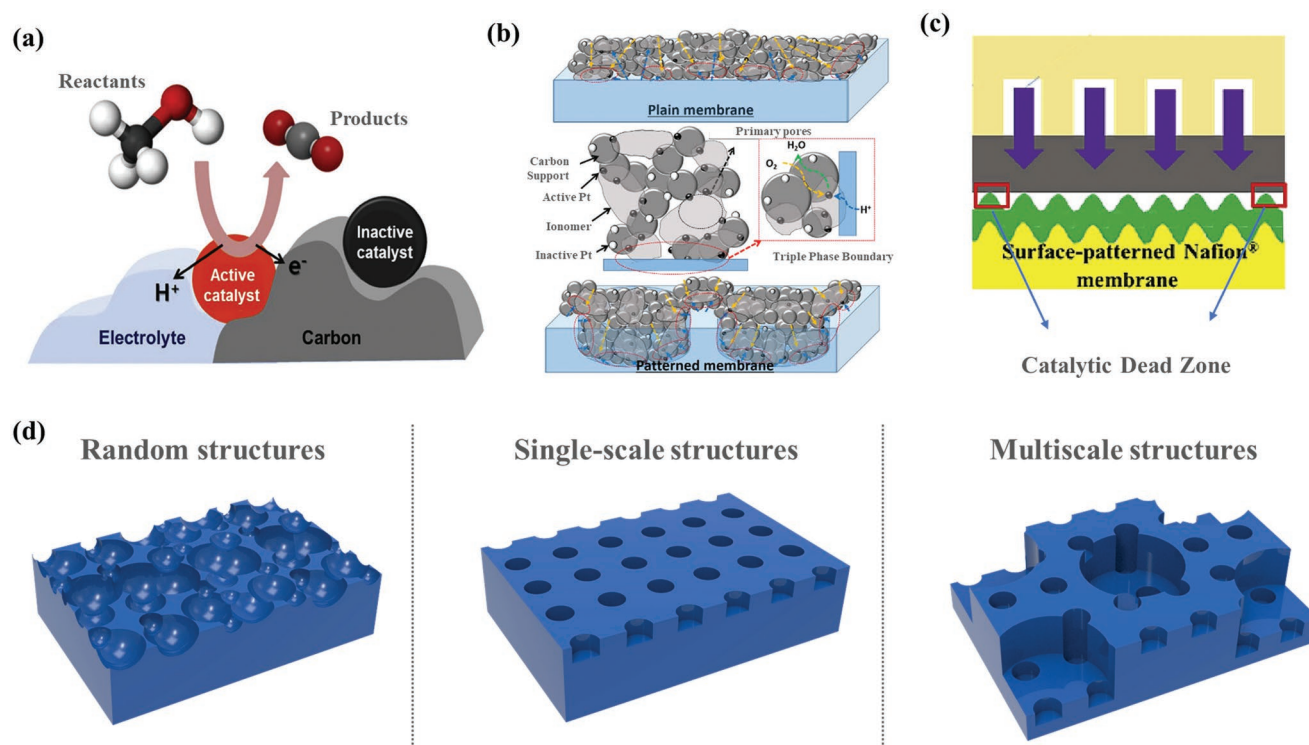


Figure 2. Schematics showing a) non-active catalyst in the electrode. Reproduced with permission.^[59] Copyright 2018, Elsevier. b) Surface patterning effects for enlarging TPB-induced high-catalyst utilization at membrane/electrode interface. Reproduced with permission.^[44] Copyright 2015, Springer Nature. c) Reduction of catalytic dead zone and facilitation of mass transport at electrode/GDL interface. Reproduced with permission.^[56] Copyright 2018, Elsevier. d) Surface-patterned membrane with random, single-scale, and multiscale structures.

the MEA, the Nafion membrane plays a critical role in water and proton transport and blocking fuel crossover. The introduction of structures on the membrane surface of the MEA can increase the interfacial contact area at the membrane/electrode, change the electrode morphology, and make the locally thinned region of the membrane as well as extrude some part of the membrane into the electrode. Previous studies indicate that the Pt-based catalyst utilized in the electrochemical reaction on the flat pristine membrane surface is less than 55% in fuel cells.^[44,45] Considering the use of the expensive catalyst, which accounts for $\approx 40\%$ of the total cost of the fuel cells, the amount of non-active catalysts in the electrode is considerable loss, as shown in **Figure 2a**.^[10,34,45] Therefore, reducing the catalytic dead zone while maximizing the triple-phase boundary (TPB) at which O_2 molecules, electrons, and protons combine (at active catalyst sites) is essential to minimize catalyst usage and improve fuel cell performance.^[46,47] The enlarging TPB-induced high catalyst dispersion and utilization at the interface between the membrane and electrode, where electrochemical reactions effectively occur, can be increased by implementing the strategy for structuring membrane surfaces (**Figure 2b**).^[15,48–53] Moreover, the surface-patterned membrane can have a considerable impact on water and ion transport through the membrane and membrane/electrode interface; this is directly related to the Ohmic resistance and charge transport resistance.^[45,54,55] Another interesting feature is that the electrode deposited on the surface-patterned membrane has a corrugated structure, thus providing a void space between the electrode and GDL.

A catalyst dead zone can be formed between the electrode and GDL under the rib area of the flow field by blocking the reactant gas to the compressed region. Hence, surface patterning can effectively reduce the catalyst dead zone at the electrode and GDL interface by transforming a 2D flat catalyst structure to a 3D curved structure (**Figure 2c**),^[56] which results in a substantial reduction in mass transport resistance.^[57,58] Now the membrane surface-patterning strategies will be reviewed by categorizing three subsections: random, single-scale, and multiscale structuring, and its impact on the device performance will also be examined (**Figure 2d**).

2.1. Randomly Distributed Nanostructures/Microstructures on Membrane

As a well-established technology in diverse applications (such as in the semiconducting industry), the plasma-induced ion bombardment technique has been adopted to generate randomly distributed nanoscale/microscale membrane roughness and reduce membrane thickness without changing the membrane's bulk chemical properties. The method offers the advantages of non-contact and one-step processing for large-area patterning.^[60–64] In 1990, the structured surface of the Nafion membrane was fabricated through a plasma process for a redox flow battery.^[65] After, a plasma-modified surface-structured Nafion membrane was used to improve the performance of PEMFCs.^[64,66–69] For membrane patterning with plasma-induced

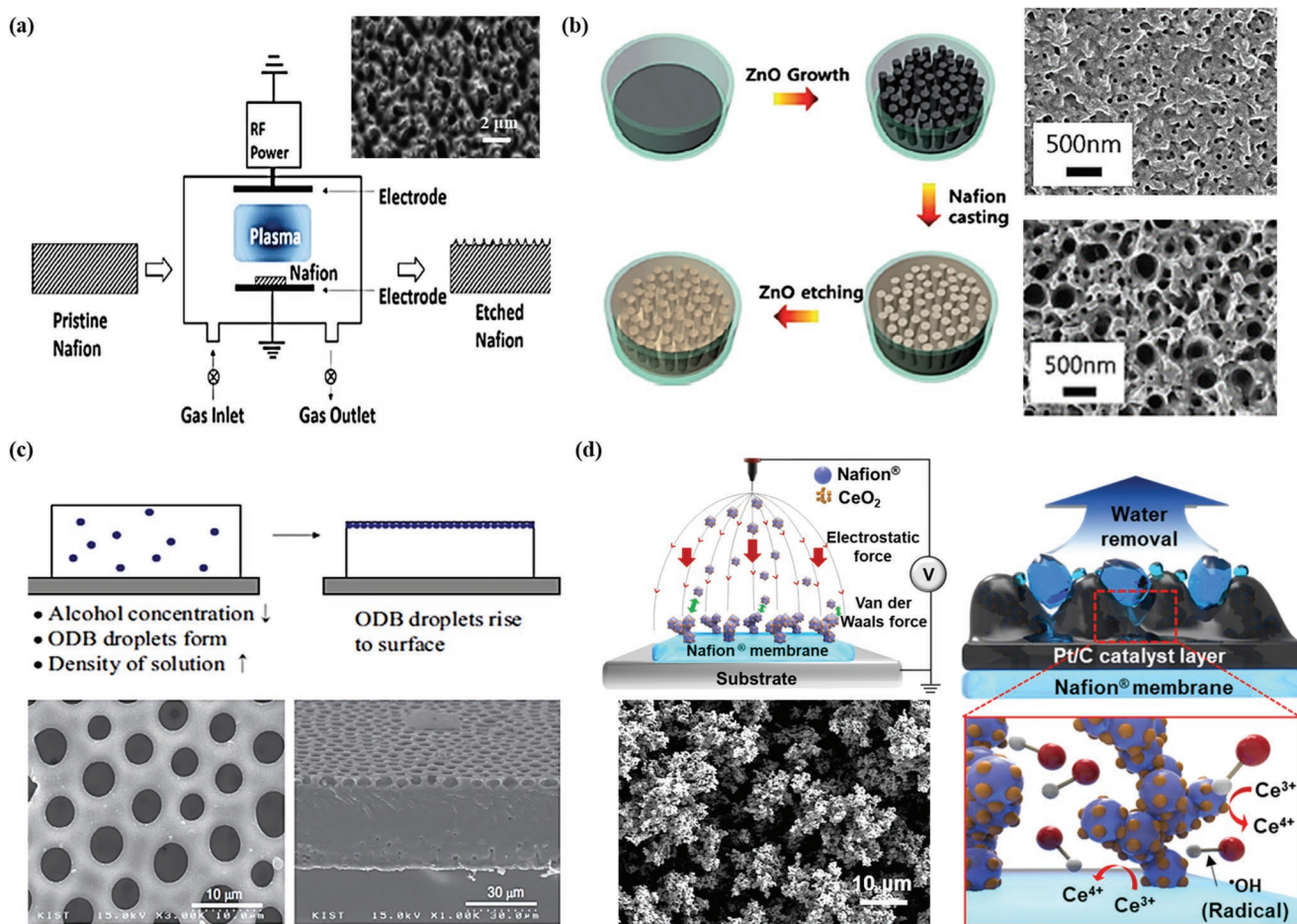


Figure 3. a) Randomly distributed nanostructures on membrane through plasma-based reactive ion etching. Reproduced with permission.^[69] Copyright 2010, Elsevier. Reproduced with permission.^[64] Copyright 2017, Wiley-VCH GmbH. b) Sacrificial ZnO templating method for constructing densely packed randomly distributed structures on membrane and SEM images with different Zn precursor concentrations of 50 (top of upper right) and 100 nm (bottom of upper right). Reproduced with permission.^[70] Copyright 2014, Wiley-VCH GmbH. c) Preparation of randomly distributed pores on membrane surface via solvent evaporation method and SEM images of surface and cross section of the modified membrane. Reproduced with permission.^[71] Copyright 2014, Elsevier. d) Construction of multifunctional Nafion/CeO₂ dendritic structures via electro-spray deposition method using a mixed solution of Nafion and CeO₂; SEM images of Nafion/CeO₂ structures. Schematics showing efficacy of modified MEA for improving water removal and alleviating radical attack. Adapted with permission.^[58] Copyright 2021, American Chemical Society.

ion bombardment, usually commercial Nafion membrane is placed in a vacuum chamber, then the gas is supplied to the chamber. The flow rates, chamber pressure, temperature, gas type (e.g., O₂, Ar, H₂, He, CF₄, and mixtures), power, frequency, and plasma-treated time are tunable (**Figure 3a**). Generally, it is believed that the process should proceed under the condition of increasing surface roughness while minimizing the loss of ion-conducting SO₃⁻ groups on the membrane surface. Cho et al.^[69] deliberately controlled the membrane thickness and surface morphology by varying the plasma etching time. The MEA with plasma-treated membrane for 10 min exhibited an increase in current density of ≈19% at 0.7 V and a decrease in the Ohmic resistance of 0.059 Ω cm² (0.072 Ω cm² for pristine Nafion 212) due to membrane thinning effect up to 40% (≈29.8 μm). Further, the increased roughness led to a reduction of interfacial resistance between the membrane and electrocatalyst agglomerates in the MEA. For leveraging the foregoing advantage of the plasma-etched membrane and

achieving ultralow Pt loading in the MEA, Besser's group sputtered Pt catalyst on the plasma-etched membrane by combining two plasma-induced compatible processes.^[64] With ultralow Pt loading (0.02 mg cm⁻²), the MEA with the etched membrane-sputtered electrode showed a much higher maximum power density (170 mW cm⁻²) compared to the MEA with the pristine membrane-sputtered electrode (138 mW cm⁻²). However, the vacuum-driven time-consuming technique for modifying the membrane surface can impede the economic viability of the PEMFCs; therefore more efforts are to be accomplished to put the plasma technique into practical use in the fabrication of the MEA.

An approach that uses sacrificial templating, mainly employing self-assembled metal oxide nanowire/rod has been reported for surface patterned membranes.^[72,73] This approach aims to provide an effective proton transport pathway and expand the interfacial contact area between the membrane and the electrode with the use of extruded Nafion array with a very

high density. For membrane patterning with sacrificial porous templates, the following preparatory steps are required: 1) Preparation of removable templates with structurally densely packed nanowire/rod. 2) Filling of the Nafion ionomer solution into the templates. 3) Thermal treatment for removing residual solvent and increasing Nafion's crystallinity. 4) Last, removing the template from the membrane with an etching solution. Shul et al. first introduced patterned-surface Nafion membranes using ZnO nanorod templates (Figure 3b).^[70] The MEA with a patterned membrane with optimized Zn precursor concentration of 100 mM exhibited a significant performance improvement (1.19 A cm^{-2} at 0.6 V) compared with the reference MEA (0.85 A cm^{-2}). The performance enhancement was ascribed to the increased ECSA values (32.59 and $55.77 \text{ m}^2 \text{ g}^{-1}$ for the pristine and patterned membranes, respectively) and a considerable reduction in charge transport resistance ($\approx 25\%$). This sacrificial templating approach is a low-cost and easy process that can significantly increase membrane surface roughness when used with the self-assembled and dense nanostructure/microstructure. However, the template is only for one-time use and the difficulty in achieving sustainable reproducibility is a critical issue for adopting this method for industrial application.

Without employing sophisticated equipment or templates, a structurally engineered Nafion membrane with a porous layer consisting of randomly distributed micro-sized pores was reported by Henkensmeier's group.^[71,74] This technique is based on a one-step solution casting method by adding a high boiling point ($\approx 180 \text{ }^\circ\text{C}$) solvent of ortho-dichlorobenzene (ODB) as a porogen in a Nafion solution. The ODB droplets rose to the surface before the membrane solidified, leading to the formation of pores with a size of $1.3\text{--}3.7 \text{ }\mu\text{m}$ in diameter (Figure 3c). The MEA with a porous surface membrane compared with that with a dense Nafion membrane exhibited a 16% higher power density under relatively high-temperature ($90 \text{ }^\circ\text{C}$) and low-humidity (relative humidity [RH]: 50%) conditions. Hence, the obtained cavity structure is presumed to act as a membrane humidifier by facilitating the back diffusion of the produced water. This one-step method is simple, but it requires careful control of process parameters such as concentration, temperature, and pressure for reproducing and controlling porous structures.

Recently, a method of forming a functional structure on the surface of a Nafion film has been reported by using electrospinning^[75] or electrospray.^[58] Generally, electrospinning techniques have been widely used to fabricate reinforced nanofiber-composite membranes from dissimilar polymers,^[76,77] and the electrospray method is employed for constructing electrodes with ultra-low catalyst loading.^[78,79] Based on the advantage of the electrospinning technique for producing polymeric fiber, Choi et al.^[75] presented a surface-patterned membrane by deposition of Nafion fiber on the membrane surface with the electrospinning method by using a mixed solution of Nafion solution and poly(ethylene oxide). The modified Nafion membrane was used for constructing a rugged electrode structure, and the MEA with modified electrode showed much higher performance at high current density region due to considerable reduction in total oxygen diffusion resistance. As a strategy to improve mass transfer by modulation of electrode shape at the same time as preventing chemical deterioration of MEA,

Jang et al.^[58] reported constructing multifunctional Nafion/ CeO_2 dendritic structures based on the electrospray method with a mixed solution of Nafion ionomer and CeO_2 dispersed solution. The CeO_2 nanoparticle is widely used as a radical quencher in PEMFC for improving chemical durability. During the electrospray deposition, the charged droplets move to the grounded substrate on which the Nafion membrane is placed, and they experienced Brownian motion and van der Waals attraction forces from the deposited particles. This resulted in self-assembled highly branched 3D porous dendritic structures on the membrane surface, and the electrode constructed on the patterned surface exhibited a bumpy surface (Figure 3d). The effects of patterned membranes are summarized as follows: 1) The 3D-highly branched dendritic structures enlarged the interfacial contact area between the membrane and electrode, which increases ECSA value. 2) Numerous void spaces between the GDL and electrode with bumps enabled the easy removal of generated water and facilitated the supply of reactant gas to the electrode. 3) The CeO_2 nanoparticles in the dendritic structure, which are located in front of the membrane, play an effective role in alleviating the chemical degradation of the MEA, and it was confirmed by performing the OCV-decay acceleration test. Although methods using electric field-assisted surface patterning show efficacy for improving MEA performance by membrane/electrode interface expansion as well as electrode structure modification, further development is necessary, such as minimizing their deposition time and securing stable discharge characteristics.

2.2. Single-Scale Patterned Membranes

Studies on diverse microelectromechanical systems (a technique for securing the precise design and reproducibility of the surface structure) have endeavored to fabricate nanoscale/microscale pattern structures on the electrolyte membrane surface.^[80–82] In the initial stages of these studies, direct patterning of the membrane using electron beam (e-beam) lithography was implemented.^[83] Omosebi et al.^[84] reported that e-beam lithography coupled with a dry etching method could fabricate a well-ordered micro-hole array ($2 \text{ }\mu\text{m}$ in diameter and $5 \text{ }\mu\text{m}$ in pitch size). The Ge layer and ZEP 520A were used as a hard mask and an e-beam resist, respectively. Successive processes of e-beam exposure, e-beam resist development, dry etching, hard mask development, and final O_2 etching were also performed. Though e-beam lithography-dry etching for constructing well-defined precise structures with high reproducibility have advantages compared to techniques used for randomly distributed structures in Section 2.1, this method has a high cost and involves complex processes, thereby limiting its large-scale application.

Thermal imprinting and solution casting using diverse structured molds have been intensively studied as efficient ways to pattern transfer while minimizing the successive etching and developing processes, which makes the surface patterning of the membrane more expensive, complex, and time-consuming.^[54–56,85,86] For membrane patterning with the thermal imprinting process, generally, the Nafion membrane is placed between the patterned mold (Si master or replicated polymeric

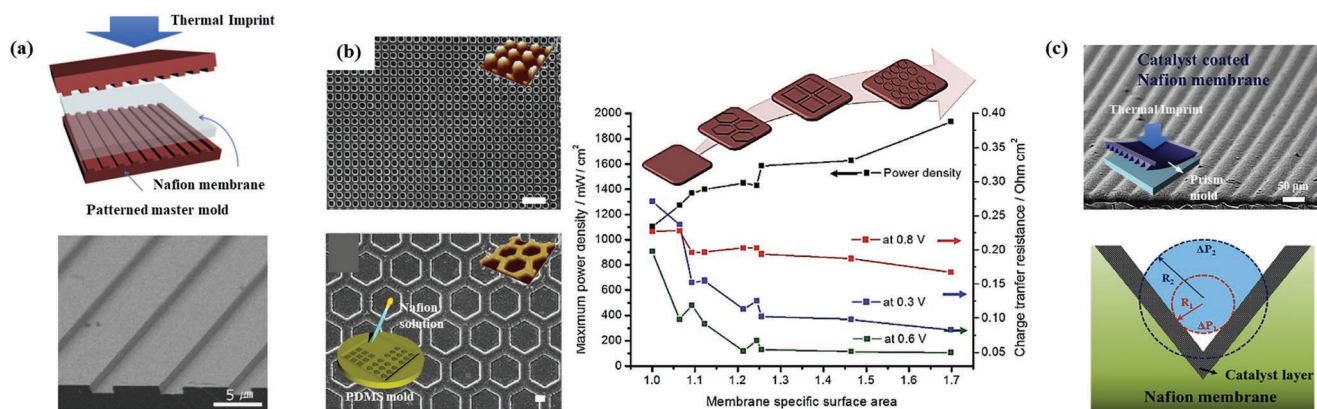


Figure 4. a) Schematic and SEM image of line patterning of membrane surface by thermal imprint method. Reproduced with permission.^[87] Copyright 2012, Elsevier. b) SEM images of patterned membranes (2- μm circle and 20- μm hexagon); maximum power density and charge transfer resistance of MEAs with patterned and plain membranes. Reproduced with permission.^[44] Copyright 2015, Springer Nature. c) SEM image of a prism-patterned array on Nafion membrane and constructed MEA by Pt/C catalyst spraying process; schematic of a water droplet in void space of catalyst layer with different curvatures at top and bottom sides. Reproduced with permission.^[57] Copyright 2016, Elsevier.

mold) and substrate, and temperature (above the glass transition temperature of Nafion ≈ 120 °C) is applied under certain conditions of pressure and time. After the modified Nafion membrane is detached from the mold and substrate, the patterned side of the membrane is generally used for the cathode side of the PEMFCs. Bae et al.^[87] presented a dual-side line-patterned Nafion membrane produced by the thermal imprint process using two-patterned Si molds without the substrate as shown in Figure 4a. Different micro- and nano-sized Si masters with width/spacing/height of 5/10/1, 5/2/1 μm , and 110/90/70 nm were used. The MEA with microline-patterned membranes exhibited improved performance (especially in the regions with high current density) due to reduced Ohmic resistance from the locally thinned membrane through dual-side micro-pattern and facilitated charge transport at the enlarged interfacial contact area (highly Nafion-loaded region due to extruded membrane part into electrode).^[88] However, interestingly, the MEA with a nanoline-patterned membrane compared with the reference MEA exhibited lower performance due to the inadequate interface between large catalyst agglomerates and nanoscale patterns (the void spaces were not fully filled with catalysts).

Although finding optimal structure through the control of surface structure design is critical for maximizing the surface patterning effect on the performance of the systemic MEA, there had not been many studies before Shul's group reported the diverse pattern effects on the MEA performance.^[44] They used a simple solution-casting method by successive steps of pouring the Nafion ionomer solution onto the patterned mold, drying out the solvent, thermal treatment, and detaching the patterned membrane from the mold. By comparing various patterned structures (i.e., circles, squares, and hexagons with different sizes between 2 and 25 μm), Shul et al. reported that a 2- μm circular pattern is mainly suitable for maximizing the MEA performance. With this pattern, high Pt utilization exceeding 80% was achieved. Moreover, the maximum performance was 1906 mW cm^{-2} under the H_2/O_2 condition with 0.4- mg cm^{-2} Pt loading; this value was 73% higher than the performance of commercial membranes with a similar thick-

ness (≈ 50 μm) (Figure 4b). They correlated this result with the largest interfacial contact area increment effect for a 2- μm circular pattern (1.73-fold compared to the flat surface). However, the square pattern showed better improved mass transfer capacity than the circular pattern with an analogous surface area increment. This is due to the macropores generated at the corners of the patterns with an angled structure. Even though the results are meaningful, it is necessary to verify whether the optimized patterns still work in large-scale MEAs in diverse operating conditions.

Macropores between the electrode and GDL generated from the patterned membrane surface are known to affect the mass transfer significantly. Hence, Kim et al.^[57] suggested a prism-patterned Nafion membrane with a V-groove electrode structure created by thermal imprinting and spraying catalyst onto the modified membrane. The MEA with a prism-patterned membrane compared with a flat membrane exhibited improved maximum power density by about 35%. The Ohmic resistance of a locally thinned membrane with micro-sized prism structures decreased by 22%, and the vertically asymmetric geometry of the V-groove electrode enhanced the water transport by reducing the mass transfer resistance (Warburg impedance) by 33.2%. They explained this structured electrode effect for water removal capacity with the generated macropore effect at the electrode and GDL interface as well as the Laplace pressure difference from the droplet radius difference in the vertically asymmetric structure (Figure 4c).

2.3. Multiscale Patterned Membranes

The multiscale engineering of membrane surface modifications for PEMFC applications has recently been reported.^[24,38,89] Multiscale hierarchical structures and combined structures with micro- and nano-scale patterns have structural advantages due to distinct micro- and nano-scale morphologies. Consequently, they have received considerable attention in diverse engineering fields, including microfluidics, surface wettability, adhesion, optics, electronics, and energy systems.^[85,90,91]

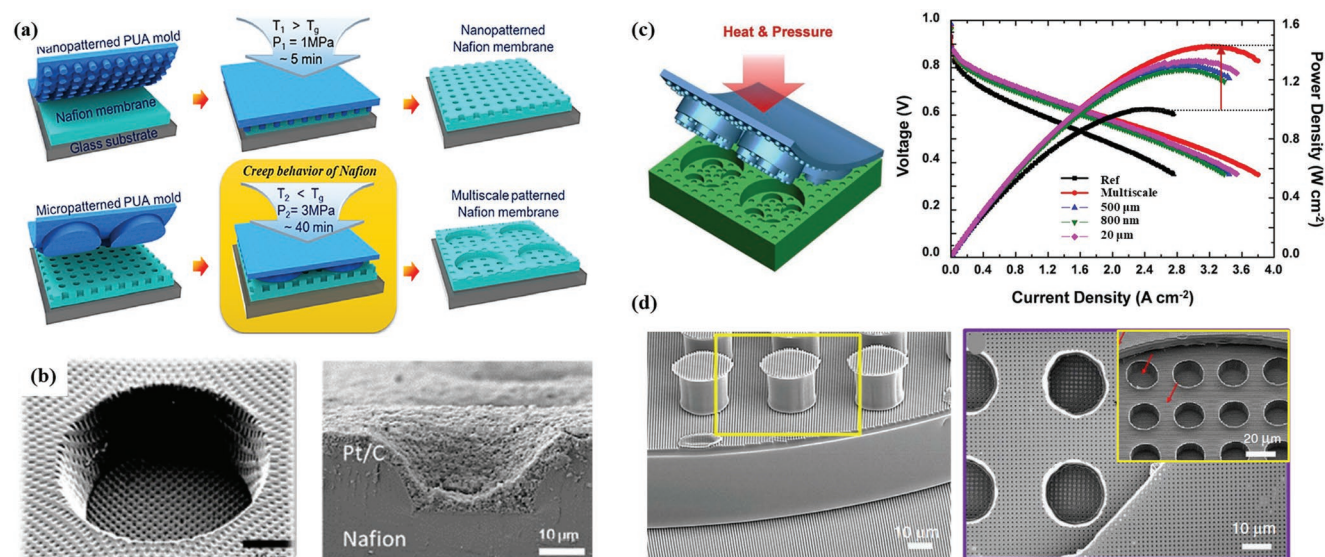


Figure 5. a) Schematic of multiscale Nafion membrane fabrication: imprinting nanopatterns on Nafion film when temperature exceeds glass temperature (T_g). Sequential imprinting of micro-patterns on nanopatterned Nafion film using creep behavior when temperature is less than T_g . b) SEM images of multiscale patterned Nafion membrane and cross section of catalyst-coated multiscale membrane. Adapted with permission.^[89] Copyright 2016, American Chemical Society. c) Schematic of multiscale multilevel patterned membrane and polarization curves of MEAs with pristine single-scale (500, 20 μm , and 800 nm) and multiscale patterned membranes supplying fully humidified H_2/O_2 at 70 $^\circ\text{C}$. d) SEM images of multiscale mold, each consisting of 500, 20 μm , and 800 nm pillars and patterned Nafion membrane. Reproduced with permission.^[38] Copyright 2015, Springer Nature.

As for fuel cell application, each multiscale structure provides mechanical stability to the thinned membrane. Catalytic utilization increases because of the further enlargement of the surface area from each single-scale structure. Moreover, the mass transport capacity improves due to the hierarchically designed structure-induced modified electrode morphology. However, the construction of multiscale structures and the transfer of the structure to the membrane surface are challenging. Hence, several researchers have suggested facile methods to construct the structure using novel lithography techniques.

Jang et al.^[89] reported a creep-assisted sequential imprinting method for fabricating a cone-shaped microstructure with nanopatterns to achieve high catalytic utilization and water removal efficiency. The authors used successive thermal imprinting using each nano- and micro-scale polymeric mold by setting the two pairs of temperature and pressure values for constructing multiscale structures: 120 $^\circ\text{C}$ and 1 MPa (conventional thermal imprinting condition) and 80 $^\circ\text{C}$ and 3 MPa (creep-assisted imprinting condition) (Figure 5a). During the second molding process, the pre-structured nanoscale pattern from the first imprinting process remained, because this process was performed at a temperature lower than the glass transition temperature of the Nafion membrane (≈ 120 $^\circ\text{C}$). At this condition, additional cone-shaped asymmetric microstructures were successively engraved by mechanical creep deformation to the membrane (Figure 5b). By utilizing the multiscale structure, the surface area was increased by 1.7 times compared to the flat surfaces due to incorporating microscale and nanoscale structures, resulting in improved catalytic utilization. With the foregoing and the aid of the asymmetric macro-void space between the electrode and the GDL inducing the Laplace pressure difference (similar to the introduced prism-patterned membrane above), the mass transport resistance was considerably reduced by 51%.

Sequential imprinting steps based on the creep behavior of Nafion have the advantage of facile creating a multiscale structure while expanding the feasible pattern shape and dimension; however, it is difficult to precisely maintain the original shape of the previously formed nanopattern, and importantly, it takes a relatively long process time to induce creep deformation of the membrane. Therefore, a technique for making a multiscale structured membrane by a one-step thermal imprinting process is required. For this, it is necessary to develop a mold having a multiscale structure in advance. Cho et al. reported the utilization of a one-step process using the multiscale multilevel polymeric mold with 800, 20, and 500 μm pillars.^[38] By stacking each 20- μm and 500- μm microstencil engraved with nanopatterns on the 800-nm hole-patterned substrate and applying ultraviolet (UV) curing for the lamination process, a multiscale tri-level negative structure was fabricated. Subsequently, the structure was replicated by pouring and curing the PDMS prepolymer. Finally, a Lego-like multiscale multilevel structure was prepared. With this mold, the Nafion membrane surface is modified, and a tri-level hole pattern with different micro- and nano-sizes is obtained by a one-step thermal imprinting process, as shown in Figure 5c. Interestingly, the patterned membrane has three different thicknesses: L_1 (≈ 50 μm), L_2 (≈ 30 μm), and L_3 (≈ 10 μm). The membrane reduced the Ohmic resistance by 16%, shortening the proton pathway in the patterned region of the membrane while securing the mechanical robustness because L_1 provides geometrical reinforcement resulting from the hierarchical leveling. Furthermore, with the tri-level structural morphology, the surface area increased by 1.96 times that of the flat surface, improving the ECSA up to 20% (69.12 m^2 g^{-1}). By combining these effects, the MEA with a multiscale multilevel membrane exhibited a high maximum

power density value of 1.4 W cm^{-2} under H_2/O_2 conditions without back pressure. Compared with the MEA with a flat membrane, it exhibited an increment of $\approx 40\%$; its performance was also higher than that of each single-scale pattern used for constructing multiscale structures (Figure 5c). In similar work with the use of a multiscale patterned mold, recently, Lee et al.^[92] reported a method for making hierarchical wrinkles patterned polymeric mold consisting of three different pattern sizes of 0.4, 3, and $10 \mu\text{m}$ by using repetitive heat-induced mechanical deformation between a stiff top skin layer and a soft bottom. The constructed pattern was replicated by PDMS mold like the previously introduced study. And they successfully exhibited much improved MEA performance with a modified Nafion membrane than that of the MEA with a pristine Nafion membrane with the advantage of superpositioned effects of each different size of three patterns for enlarging interfacial area between the membrane and the electrode.

2.4. Summary of Surface Patterned Membrane Approach

The membrane–electrode interface and electrode morphology modification through the multiscale engineering of the membrane surface using the same existing materials can improve the fuel cell performance by employing structural effects, and multiscale structure can further exploit combinational advantages of each single-scale structure.

When examining the effect of surface patterning from the point of view of voltage loss, the effects of surface patterning are summarized as follows:

- 1) Effective utilization of the catalyst through the expansion of the membrane/electrode can reduce the activation overpotential by increasing the ECSA value despite using the same amount of catalyst in the MEA. This can be explained by Equation (2) with the increase of L_C (the effective catalyst loading per unit area, g cm^{-2}). However, when explaining the increase of catalytic utilization, most studies focused on the calculation of ECSA values from the CV measurements while omitting critical analysis of reduction in activation overpotentials such as impedance analysis at low current density region with equivalent circuit model and Tafel slope analysis.
- 2) Locally thinned regions in the patterned membrane can reduce proton transport resistance in the membrane, as well as the extruded part of the Nafion membrane inside the electrode makes the higher Nafion ionomer loading at the interface result in the reduction of the proton transport resistance at the interface between the membrane the electrode. This can lead to the reduction of Ohmic overpotential represented in Equation (3). However, since the effects of R_{mem} and $R_{\text{H}^+, \text{CL}}$ resistance cannot be easily obtained from high-frequency resistance (HFR) in EIS spectra alone, it is required to measure other techniques such as through-plane proton transport resistance of the membrane and H_2/N_2 EIS measurements based on the transmission-line model for proton transport resistance in the electrode.^[93]
- 3) Change in the shape of the electrode due to the micro-sized pattern and the formation of macro voids at the electrode/GDL interface can lead to a decrease in mass transfer resistance, especially in the high current density region. This results in the change of pore structure in the electrode and electrode/GDL interface to be effective for easy removal of water and improving oxygen transport, which is related to the change of ε (porosity) shown in Equation (5). For calculating the oxygen transport resistance independently from water generation, employing methods such as limiting current measurement with diluted O_2 or H_2 gas can be an excellent way to explain the enhancement of mass transfer.^[94]

The summarized values from each surface patterning study for ECSA, Ohmic resistance, and mass transport resistance are shown in **Table 1**. The Ohmic and mass transport resistance can be extracted from HFR and low-frequency resistance (LFR) subtracted by HFR (LFR–HFR) in EIS spectra, respectively. And for a better visual understanding, the graphs were plotted by selecting the representative studies that clarified the pattern size, surface area increment, operating condition, and electrochemical key values (**Figure 6**). First, regarding the relationship between the ECSA change and the surface area increment, the case of the nanosized pattern ($\approx 250 \text{ nm}$) showed a rather decrease in ECSA value. This is because Pt/C catalyst agglomerates could not fill the inside of the nanosized pattern, so the contact between the membrane and the electrode was not properly made. And this brought poor results for other HFR, LFR–HFR, and peak power densities. Though the ECSA change was observed to increase as the surface area increased in single- and multi-scale structures, the ECSA increase rates are quite different for each membrane pattern study, even under similar pattern shapes and surface area increments. Therefore, to more accurately quantify the effect of each pattern for ECSA increment, it is recommended to carefully perform the CV measurements for interpreting ECSA values because CV measurement is quite sensitive to experimental errors and experimental conditions such as nitrogen purge rates at the working electrode.^[95] And the authors need to describe the detailed information of the ionomer, catalyst, their composition in electrode, and MEA fabrication method for precise comparison of surface patterned effects on the ECSA. In the case of LFR–HFR at a high current density region, the influence of the actual kinetic charge transfer resistance is negligible, which means the values of LFR–HFR are determined mainly by mass transport limitations. Except for the nanosized pattern mentioned above, it was found that the mass transfer resistance decreased as the surface area increased in single-scale structures as well as superpositioned surface area increment in multiscale structures. Therefore, it can be seen that gas transport and water management are improved, and this led to better Pt utilization in the high current region. When it comes to HFR reduction which is related to Ohmic resistance, it was confirmed that the patterned membrane produced through solution casting showed a more significant reduction in Ohmic resistance than the modified membrane through thermal imprint using the existing commercial Nafion membrane. Considering that thermal

Table 1. Membrane surface patterning methods and their effects on performance.

Type	Feature	Size ^{d)} [μm]	Enlarged Surface	Mem. Thick. [μm]	ECSA [imp.] [m ² g ⁻¹ [%]]	HFR [Reduc.] [mΩ cm ² [%]]	HFR-LFR [Reduc.] [mΩ cm ² [%]]	Max. Power [Imp.] [mW cm ⁻² [%]]	Cathode Pt [mg cm ⁻²]	Area [cm ²]	Operating condition	Notes	Ref.
Random													
Plasma	Random roughness	0.14 Rough.	—	Nafion 212 51 → 49.5	—	118.4 (−41)	287.7 (+31)	514.6 (+23)	0.1	16	H ₂ /O ₂ , 60 °C 100 kPa _{abs}	EIS at 0.6 V	[64]
	Random roughness	—	—	39.7 → 29.8	17.2 (−15)	56 (−18)	207 (−1)	558 (+12) ^{a)}	0.2	5	H ₂ /Air, 70 °C 100 kPa _{abs}	EIS at 0.6 V	[69]
	Random roughness	0.087 Rough.	—	Nafion 115	—	—	—	620 (+107)	0.2	25	H ₂ /O ₂ , 80 °C 100 kPa _{abs}	—	[68]
Sacrificial template	Nanofiber	0.2/10 (D/L)	—	Casted 40	10 (+54)	—	—	26 (+100) ^{a)}	0.089	1	H ₂ /Air, 80 °C 250 kPa _{abs}	—	[73]
	Nanorod	—	—	Casted 47.2	55.77 (+71)	111 (−4)	104 (−25)	950 (+59)	0.4	1	H ₂ /O ₂ , 75 °C 100 kPa _{abs}	—	[70]
Solvent evaporation	Porous	1.3–3.7 (D)	—	Casted 33	134 (+168)	—	571 (−26) ^{c)}	356 (+10) ^{b)}	0.4	25	H ₂ /Air, 95 °C 100 kPa _{abs}	EIS at 0.8 V	[71]
Electric-field	Dendritic	8 (L)	—	Nafion 211 25 → max. 33 ^{c)}	51.1 (+34)	61 (+3)	193 (−14)	685 (+9)	0.2	5	H ₂ /Air, 70 °C 100 kPa _{abs}	EIS at 0.6 V	[58]
	Rugged	3 (D)	—	Nafion 211 25 → min. 25 max. 31 ^{c)}	66 (−0)	59 (0)	516 (−52)	508 (18) ^{a)}	0.15	25	H ₂ /Air, 80 °C 180 kPa _{abs}	EIS at 1 A cm ⁻²	[75]
Single-scale													
Thermal imprinting	Pillar	7/10 (W/H)	2.8	Casted 40 ± 2	—	—	—	310 (+15)	0.3	36	H ₂ /Air, 90 °C 150 kPa _{abs}	—	[96]
	Line	5/10 (W/S)	1.13	Nafion 212 50 → min. 49 ^{c)} max. 50	32.4 (−2)	67 (−15)	193 (−7)	610 (+9)	—	—	—	—	—
		5/2 (W/S)	1.29	Nafion 212 50 → min. 49.93 ^{c)} max. 50	32.3 (−2)	61 (−23)	191 (−8)	700 (+25)	0.2	5	H ₂ /Air, 70 °C 100 kPa _{abs}	EIS at 0.6 V	[87]
		0.11/0.09 (W/S)	1.70	—	32.8 (−0)	83 (+5)	207 (−0)	500 (−11)	—	—	—	—	—
	Prism	50/25 (S/H)	1.41	Nafion 212 50 → min 25 ^{c)}	59.94 (+3)	66 (−22) ^{c)}	190 (−27) ^{c)}	720 (+50)	0.12	5	H ₂ /Air, 80 °C 100 kPa _{abs}	EIS at 0.6 V	[57]
2 (D)		1.70	Casted 45	67.86 (+69)	43 (−55)	50 (−55)	800 (+37) ^{c)}	—	—	—	H ₂ /Air, 75 °C 100 kPa _{abs}	—	—
Solution casting	Circle	—	—	—	—	—	—	1906 (+73)	0.4	1	—	EIS at 0.6 V	[44]
		3 (D)	1.47	Casted 46	61.94 (+54)	56 (−42)	51 (−54)	1629 (+48)	—	—	—	H ₂ /O ₂ , 75 °C 100 kPa _{abs}	—
	—	5.5 (D)	1.26	Casted 48	56.09 (+40)	57 (−41)	54 (−51)	1584 (+44)	—	—	—	—	—
	—	7 (D)	1.244	Casted 48	57.04 (+42)	65 (−32)	67 (−40)	1430 (+30)	0.4	1	H ₂ /O ₂ , 75 °C 100 kPa _{abs}	EIS at 0.6 V	—
	Line	3/5 (W/S)	1.19	Casted 50.3	58.2 (+46)	80 (−33)	50 (−50)	1260 (+59)	—	—	—	—	—
		8/10 (W/S)	1.08	Casted 50.5	51.2 (+28)	90 (−25)	80 (−20)	1040 (+32)	—	—	—	—	—
17/20 (W/S)		1.04	Casted 50.1	45.1 (+13)	110 (−8)	80 (−20)	980 (+24)	0.4	1	H ₂ /O ₂ , 75 °C 100 kPa _{abs}	—	[45]	
—	0.25/0.35 (W/S)	1.22	Casted 49.1	32.6 (−19)	120 (0)	120 (+20)	750 (−5)	—	—	—	—	—	

Table 1. Continued.

Type	Feature	Size ^{d)} [μm]	Enlarged Surface	Mem. Thick. [μm]	ECSA [imp.] [m ² g ⁻¹ [%]]	HFR [Reduc.] [mΩ cm ² [%]]	HFR-LFR [Reduc.] [mΩ cm ² [%]]	Max. Power [Imp.] [mW cm ⁻² [%]]	Cathode Pt [mg cm ⁻²]	Area [cm ²]	Operating condition	Notes	Ref.	
Multiscale														
Sequential imprinting	Circle (single-scale)	0.8 (D)	1.46	—	—	—	—	662 (+2) ^{c)}	—	—	—	—	—	
		40 (D)	1.24	—	—	—	—	692 (+6) ^{c)}	0.12	5	H ₂ /Air, 80 °C 100 kPa _{abs}	—	[89]	
	Hierarchical circle (multiscale)	40/0.8 (D)	1.7	Nafion 212 50 → avg. 48	68.07 (+7)	65 ^{c)} (-7)	278 ^{c)} (-33)	721 ^{c)} (+11)	—	—	—	EIS at 0.5 V	—	
Multiscale mold	Circle (single-scale)	0.8 (D)	1.79	—	—	—	—	1257 (+26) ^{c)}	—	—	—	—	—	
		20 (D)	1.75	—	—	—	—	1321 (+32) ^{c)}	—	—	—	—	—	
	Hierarchical circle (multiscale)	500/20/0.8 (D)	1.96	Nafion 212 max. 50 50 → mid. 30 min. 10	69.12 (+20)	71 ^{c)} (-16)	228 (-12) ^{c)}	636 (+33) ^{c)}	1423 (+42)	—	—	H ₂ /Air, 80 °C 100 kPa _{abs}	EIS at 0.6 V	—
		Wrinkle (single-scale)	3 (S)	1.76 ^{c)}	—	81.5 (+62)	57 (-10) ^{c)}	212 (-37) ^{c)}	390 (+48) ^{c)}	—	—	—	—	—
		Hierarchical wrinkle (multiscale)	10/3 (S)	2.46 ^{c)}	Nafion 211 N/A	92.37 (+83) ^{c)}	—	197 (-42) ^{c)}	410 (+56) ^{c)}	0.05	12.25	H ₂ /Air, 65 °C 180 kPa _{abs}	EIS at 0.5 A cm ⁻²	[92]
		10/3/0.4 (S)	3.85	—	95.2 (+89)	54 ^{c)} (-14)	168 (-50) ^{c)}	440 (+67)	—	—	—	—	—	

^{a)}Value based on 0.6 V current density; ^{b)}Value based on 0.4 V current density; ^{c)}Estimated value from graph/paper; ^{d)}D: diameter, L: length, W: width, S: spacing, H: height.

imprinting has more advantages in terms of reproducibility and process efficiency for commercialization, it is seen that the HFR can be reduced by 7–23% through micro-sized and multiscale patterns by modifying the membrane with the thermal imprinting technique. In addition, the reduction in HFR does not have a linear relationship with the size of the pattern; therefore, it is desirable to select the proper pattern dimension by considering the surface area increment as well as the thickness of the membrane being used. Last, the peak power density increased the most at the pattern size of 2–20 μm in the single-scale pattern (the shaded range). In the case of the multiscale patterns, it was observed that the increments were larger than each single-scale pattern. Considering the recent trend of using thin electrolyte membranes (10–25 μm) for high-performance PEMFCs, it is inferred that a pattern with a height of 10 μm or less and a small diameter is advantageous for HFR reduction. And a multiscale architecturing strategy within that size range is most desirable to maximize the interface expansion effect and exploit each single-scale pattern effect.

3. Electrode Modification

The fuel cell electrode referring to the catalyst layer is the key component to generating electricity from electrochemical reactions. Generally, the electrodes are made of a porous mixture of carbon-supported platinum and ionomer, and this porous

electrode structure is useful to maximize ECSA and mass transport capacity. In the electrode, catalyst particles not only contact both protonic and electronic conductors for catalytic reactions, and that place for the reaction is called TPB. At the cathode electrode, generated water can help improve proton conductivity through ionomer hydration, but the TPB can be blocked by excessive water film. It means balancing between removing the product (i.e., water) from the TPB and supplying reactant gas (i.e., oxygen) for improving mass transport is a critical issue. In the aspect of the development of a highly active catalyst itself, substantial efforts have been devoted to improving the electrochemical activity of ORR catalysts (mainly carbon support-based Pt) by manipulating their shape, size, and composition, leading to a remarkable increase in catalytic activity.^[97–99] However, most studies have verified the performance of catalysts using liquid-based half-cells with an extremely thin electrode immersed in a liquid electrolyte. Consequently, when these catalysts were applied to the MEA in a single-cell assembly with a solid electrolyte membrane, they exhibited considerably lower performance compared with that of the same catalysts used in a half-cell test.^[100] This discrepancy is due to the differences in experimental conditions. For the half-cell test, the ion transport occurs from a liquid electrolyte rather than a solid-phase ionomer, therefore, the ion transport in the thin electrode is fast and the transport resistance could be negligible. In addition, the half-cell experiment is usually conducted under the O₂ saturated liquid electrolyte, so the mass transfer resistance is not severe and not significantly

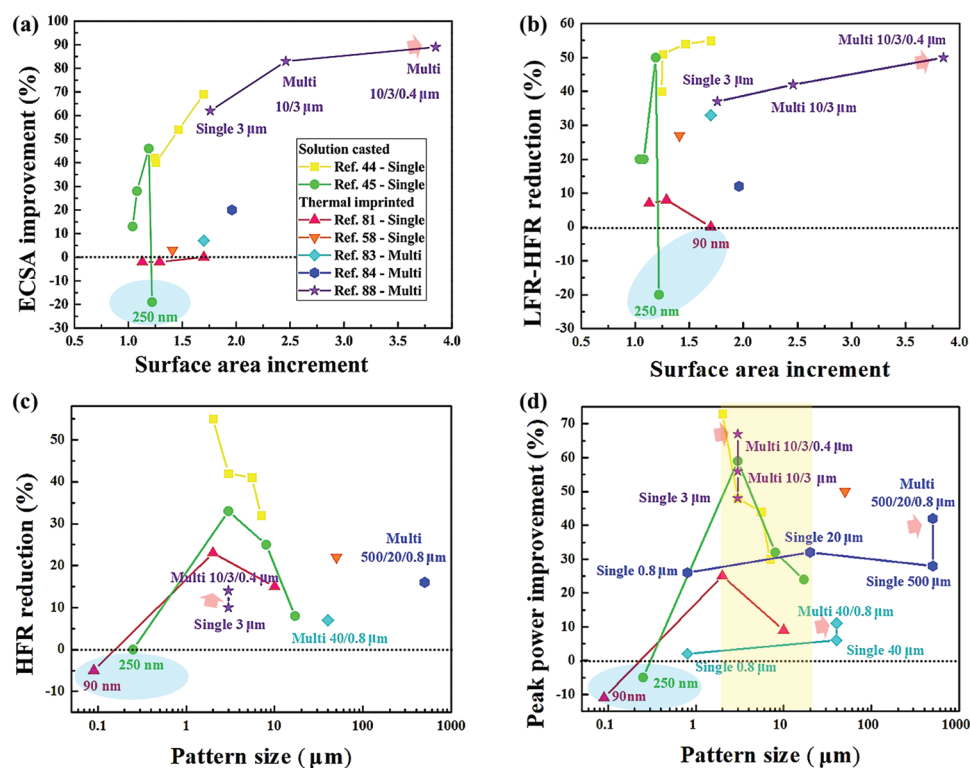


Figure 6. Comparison of membrane surface patterning effects for a) ECSA, b) HFR-LFR, c) HFR, and d) Peak power density.

considered. However, in the actual single-cell operation, the electrode is relatively thick (several micrometers or more) compared to that of the half-cell test. Hence, both the ion transfer resistance through the ionomer phase and the reactant O_2 supply (mass transfer) to the TPB in thick electrode should be importantly considered. Due to these additional resistances, generally, the utilization of Pt catalyst in MEA conditions is much lower than that of the half-cell test. And based on the fact the reactants and products are transported through the pores in the electrode, the morphology, distribution, and size of the pores greatly affect the transport behavior and the MEA performance. Therefore, in addition to developing novel catalysts, a structural engineering method for the electrode from a systemic point of view (such as ion conduction, reactant gas transfer, and water management in the MEA) must also be devised to improve the practical performance of fuel cells. Accordingly, studies on optimizing the electrode structure to maximize the utilization of the catalyst and improving mass transfer while minimizing catalyst usage have been reported in the aspect of lowering the $\eta_{kinetic}$ values by increasing the number of available active sites (Equation (2)) of catalysts and the η_{mass} by changing the pore-structure and porosity (ϵ) as well as reactant transport path length (Equations (4) and (5)). Furthermore, durability and reliability issues that inherently occur due to the degradation of the catalyst support material (e.g., carbon nanoparticle) can be addressed by architecturing strategies with supportless multiscale structured catalysts. These investigations are mainly divided into two parts: 1) electrode pore structure and 2) 1D or 3D electrode architecture studies.

3.1. Pore-Controlled Electrodes

Generally, the electrodes in PEMFCs are 1–20 μm thick and consist of Pt/C catalysts and a proton-transporting ionomer binder (e.g., Nafion ionomer). Fuel cell performance considerably depends on proton and electron conduction, reactant gas (H_2 and O_2) transport, and water management.^[101] To enhance the oxygen transport in thick electrodes, the structure of electrodes is typically tailored to secure macropores (pores exceeding 50 nm in size) using pore-forming agents by lowering the tortuosity of gas diffusion and alleviating water clogging, which hampers the oxygen access to active sites.^[102–104] From Watanabe's work,^[105] the electrode consisting of Pt/C and ionomers has two types of pores with different size distributions. The smaller pores are "primary pores," formed in the spaces between the primary carbon support particles (aggregates) with typical sizes of 10–100 nm. These aggregates form larger structures (>100 nm), called agglomerates, and larger pores, defined as "secondary pores" formed between the agglomerates. It is reported that the primary and secondary pores area act as reaction areas and gas-diffusion paths in the electrode. Particularly, the secondary pores with a pore size of 100 nm or larger determine mass transport resistance such as O_2 supply and water management. Based on this, it is obvious that as the amount of large secondary pores increases, the electrode structure becomes more advantageous for alleviating mass transport limitation at the cathode. Therefore, many studies have been conducted to increase the ratio of secondary pores corresponding to the macropore size region using various types of pore-forming agents such as magnesium oxide (MgO), Li_2CO_3 , ammonium

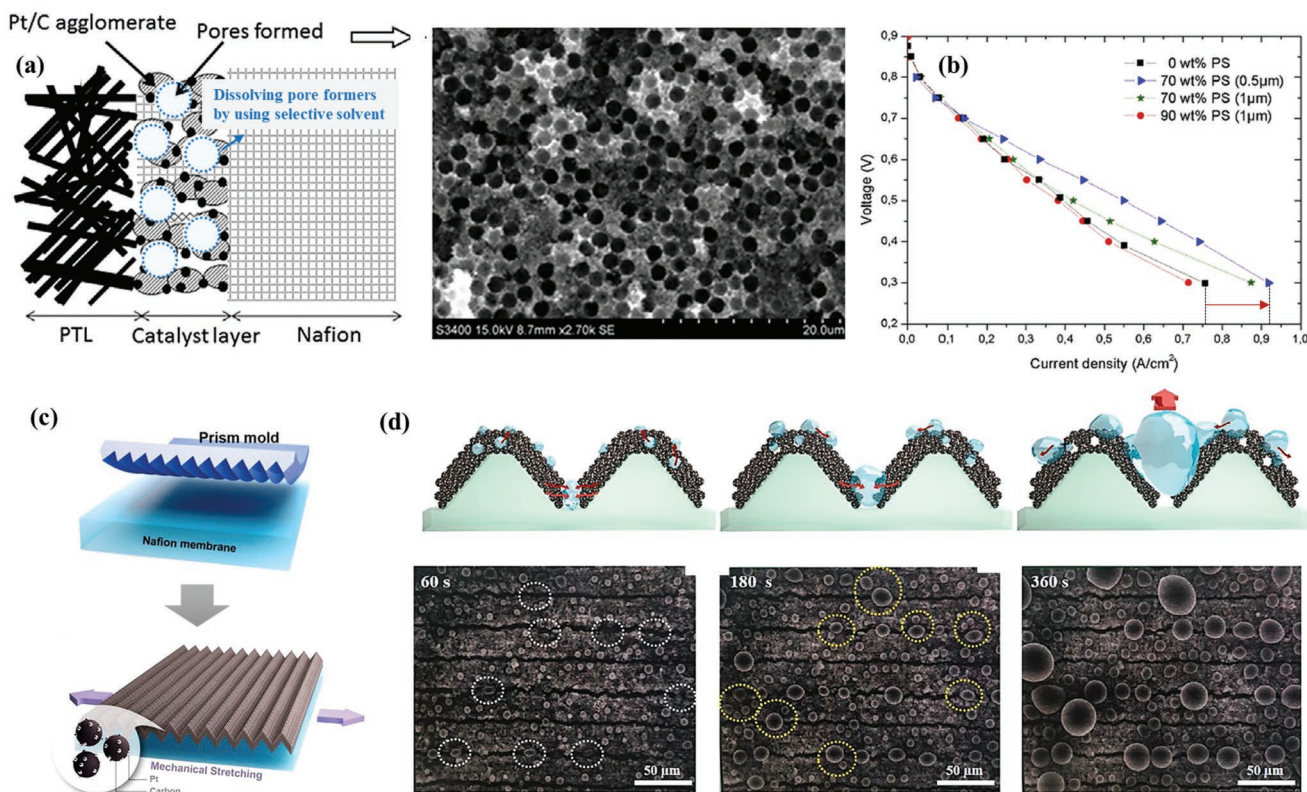


Figure 7. a) Schematic of MEA cross section with pores formed in cathode; SEM images of surface of cathode catalyst layer with 1- μm pores resulting from removal of 70 wt% monodispersed PS particles (volume ratio: 52%). Reproduced with permission.^[112] Copyright 2015, Elsevier. b) Polarization curve comparing performance between reference MEA (0 wt% PS) and MEAs with micrometer-sized pore formers (0.5- and 1- μm spheres) of various percent weight values. c) Schematic of MEA with guided electrode cracks. d) Behavior of generated water in cracks in catalyst layer; E-SEM images of water behavior on 20- μm cracked catalyst layer (strain \approx 0.5) with respect to time: 60, 180, and 360 s; chamber pressure and substrate temperature were maintained at \approx 5.1 Torr and \approx 2 °C, respectively (95% RH). Reproduced with permission.^[24] Copyright 2018, Springer Nature.

carbonate, bicarbonate, oxalate, and MWCNT.^[106–111] Among the related studies, Zlotorowicz et al.^[112] used monodispersed PS particles (0.5 and 1 μm in diameter) as pore formers, tailoring the macroporous volume fraction of cathode electrodes between 0 and 0.58 (Figure 7a). The catalyst ink with PS particles was sprayed on Nafion 212 with a layer thickness of 1 μm ; all PS particles were removed by washing with ethyl acetate. This led to a significant reduction in Pt loading and the introduction of additional macropores (0.040–0.065 mg cm^{-2} with a PS volume fraction of 0.58–0.31) in contrast to that of the reference MEA without a pore former (0.11 mg cm^{-2} with no PS volume fraction). Under the fully humidified condition of the cathode (Figure 7b), the MEA with additional pores (0.5 μm in diameter and 0.52 in volume fraction) has low Pt loading (0.047 mg cm^{-2}). Nevertheless, it showed an improved power density value of 33% at 0.6 V (0.20 W cm^{-2}) compared with that of the reference MEA with Pt loading (0.11 mg cm^{-2}) due to the enhanced oxygen transport in the electrode. In a similar study, Cheng et al.^[113] presented a modified MEA design with a dual-layered cathode using MgO as a pore former. The oxygen diffusivity ($11.6 \times 10^{-4} \text{ cm}^2 \text{ s}^{-1}$) was two times higher, and the peak power density of the pore-formed electrodes increased by 36% compared with those of the original electrodes.

Kim et al. introduced the novel method of the creation of macropores via mechanical stretching-induced crack generation

without using a pore former, which required the removal of the agent after the fabrication of the MEA.^[31] Generally, cracks are considered defects in fuel cells. Under hygrothermal cyclic operating conditions, mechanical stress is induced, and cracks that severely affect the durability of the MEA are generated. However, the authors intentionally introduced predefined cracks with periodicity to the electrode by mechanically stretching the MEA before operating the fuel cells; therefore, these generated cracks considerably differ from those induced by the MEA degradation. Compared with the reference MEA with the original electrodes, the MEA with cracks and a stretching ratio of 1.5 showed higher maximum power density (\approx 22% [0.72 W cm^{-2}]) as well as better durability and performance even after repeated polarization tests (1000 cycles). Ahn et al.^[24] devised a guided cracking strategy through the mechanical stretching of the MEA where the catalysts were deposited on the prism-patterned membrane. This enabled them to observe the water behavior on the cracked electrode as well as manipulate the crack size and improve the reproducibility of the crack morphology. Cracks were generated only in the valley of the prism structures using stress concentration effects (Figure 7c). Based on environmental scanning electron microscopy measurements (Figure 7d), the water droplet behavior was successfully observed and it can be represented in three steps. First, the water generated inside the electrode moves to the

surface of the electrode and into the cracks. Then, it coalesces with neighboring droplets and liquid water filling the cracks. Finally, droplets emanating from the cracks increase in size and are ejected to the GDL. Therefore, the cracks in the electrodes act as efficient water reservoirs and liquid water passages, and the MEA with a guided cracked layer (pitch size: 20 μm ; crack width: 2 μm), which had the highest crack density, showed a higher maximum power density ($\approx 863 \text{ mW cm}^{-2}$) than the reference MEA ($\approx 730 \text{ mW cm}^{-2}$).

Although the advantages of structural modification of pores have been demonstrated by many researchers, various technical issues need to be addressed. First, the introduction of additional pore formers inevitably complicates the MEA manufacturing process including removal steps, which results in an increase in production price in turn. In addition, during the removal process, the MEA components such as membrane, catalyst, carbon, and ionomer could be damaged by the chemicals, and their performance can be deteriorated by the adsorbed residues without being completely removed. Also, there is a high possibility that the mechanical strength of the electrode decreases due to pore formers. Since pore-forming inevitably generates more void space than the conventional electrode, mechanical deformation during the compression in the cell assembly process and repetitive contraction/swelling behavior during fuel cell operation (such as the freeze/thaw cycle) may induce the structural collapse of the pores, which leads to the failure of the key function of the generated pores. In the case of intentional crack generation strategies, it is very challenging to perfectly control the size and morphology of cracks in the large-area electrode, and if the size of generated cracks is too large, interconnection problems between catalysts may occur and induce in-plane direction ion or electron transfer issues.^[114]

3.2. 1D Structured Electrode Structures

Different from the typically used 2D flat structure of electrodes, the structural engineering approach for modifying the electrode to have vertically aligned 1D or 3D structures has been reported to achieve low Pt usage and maximize the mass transport capacity of the MEA.^[115,116] The effective charge transfer of electrons and protons as well as the mass transfer of gas and transport of liquid water can be enabled by a 1D-ordered electrode structure with vertically aligned channels.^[117] Accordingly, significant efforts have been devoted to the fabrication of 1D electrodes, including Pt nanowire arrays (NWAs),^[118] carbon nanotube (CNT) arrays,^[30] bimetallic nanotube arrays,^[119] and conductive polymer NWAs.^[120] Toyota has fabricated vertically aligned CNT (VACNT) electrodes, as shown in **Figure 8a**. A vertically aligned 1D structure can enhance gas diffusivity, water drainage, and Pt utilization. In addition, as a supporting material, CNTs improve the resistance against electrochemical oxidation at high potentials owing to their graphitic lattice structures.^[30] The fabricated electrode, decal-transferred to the membrane, has low Pt loading (0.1 mg cm^{-2}) and is 8 μm thick (in a cell). The superiority of the VACNT electrode over the conventional Pt/C electrode in the large-area 236- cm^2 cell was exhibited by the remarkably high current density (2.6 A cm^{-2} at 0.6 V). Moreover, the power output per Pt unit mass of

10.4 kW g^{-1} (reported when the paper was published in 2014) already surpassed the 2017 US DOE target of 8 $\text{kW g}^{-1}_{\text{Pt}}$.

As shown in Toyota's report, the Pt nanoparticles are dispersed on the surface of the support materials to minimize their usage, maximize the number of active sites, and inhibit the agglomeration among nanoparticles. However, these nano-sized Pt catalysts do not form an electrode structure by themselves when they are used in each electrode in MEAs; therefore, support materials are required. In general, carbon with a large specific surface area is commonly used as a support material because it excellently disperses nanocatalysts on its surface and has satisfactory electrical conductivity; these are vital for the construction and operation of PEMFCs.^[123] Although carbon materials are advantageous as nanocatalyst support, they have practical inadequacies, such as electrochemical corrosion problems during the startup and shutdown of PEMFC. During startups and shutdowns or fuel starvation situations in PEMFC operation, high electrode potentials exceeding 1.0 V versus RHE occur, inducing severe carbon corrosion and resulting in the collapse of the electrode structure. In addition, it can cause the detachment of Pt nanoparticles and Ostwald ripening, inducing a significant loss in ECSA.^[124] Owing to these limitations, research on various robust supports has been conducted.^[125] Research on integrated structural catalysts in which the catalyst functions as both electrocatalyst and electrode without using support materials has also been conducted. The sizes of these supportless catalysts range from hundreds of nanometers to tens of micrometers. As 1D structured materials, Pt nanotubes (NTs) have attracted considerable attention because of their well-defined, freestanding, and highly dispersed Pt structure from 1D geometry. Compared to other materials, such as 0D spherical catalysts, Pt NTs have preferentially exposed Pt facets, high aspect ratios, and improved electron transport owing to their anisotropic growth. Recently, an ultrathin self-supporting ionomer-free 1D electrode consisting of concave nanotrough-like Pt NTs was developed to facilitate proton and mass transfer as well as to drain the generated water (**Figure 8b**).^[121] The 1D nanotrough-like Pt structure was developed using sacrificial polyvinyl alcohol (PVA) nanofibers through electrospinning and the successive sputtering deposition of Pt onto the convex surface of the fiber. The morphological features of the fabricated 1D nanotrough-like Pt structures are shown in **Figure 8b**. The MEA with 1D electrode exhibits a high peak power density (22.26 $\text{W mg}_{\text{Pt}}^{-1}$), which is 1.27-times higher than that of the conventional Pt/C electrode. This is due to the facilitated mass transport capacity based on 1D structured electrodes with widely open, low-tortuosity, and short-diffusion pathways. In addition to performance enhancement, the nature of the carbon support-free electrode contributed to the remarkably improved electrode durability during the 5000 and 10 000 ADT cycles. In studies on 1D platinum alloy catalyst electrodes, Yi et al. reported the preparation of PtCo NTAs by template-assisted deposition and etching, as shown in **Figure 8c**.^[119] By employing a hydrothermal process followed by magnetron sputtering and thermal annealing, the NWA templates were synthesized. Then, the PtCo NTAs were transferred to Nafion 212, and the MEA was acid-washed. Because of the open-walled structure of the PtCo NTAs from the template etching process (**Figure 8c**), both the interior and exterior surfaces of the catalyst can be involved

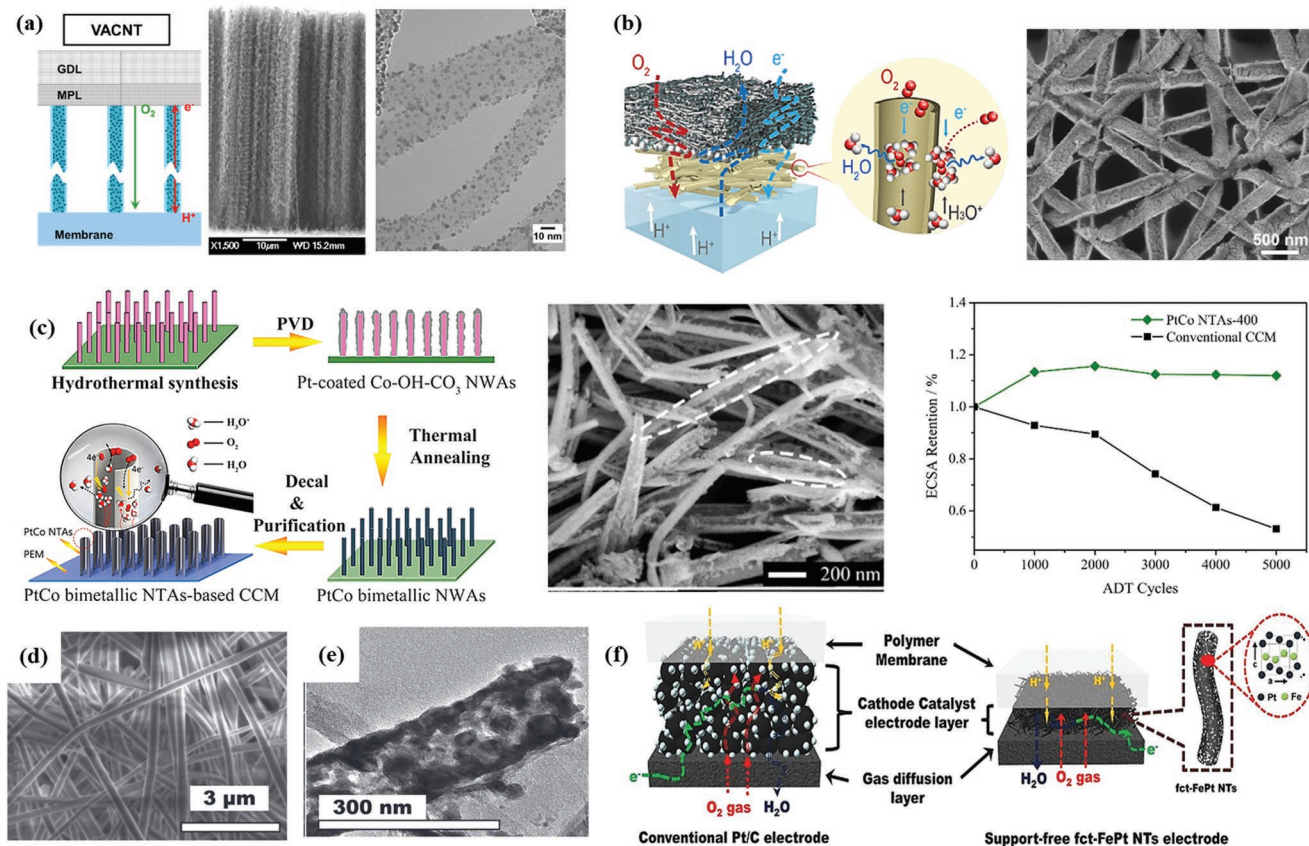


Figure 8. a) Concept of VACNT electrodes; SEM image of VACNTs and TEM image of Pt particles on CNTs. Reproduced with permission.^[30] Copyright 2014, Elsevier. b) Conceptual diagrams of Pt nanorough electrode and SEM image of Pt nanorough catalyst layer. Reproduced with permission.^[121] Copyright 2021, Elsevier. c) Schematic of fabrication process of PtCo bimetallic NTAs (left); SEM image of PtCo bimetallic NTAs incorporated into membrane (middle); ECSA retention for catalyst-coated membrane (CCM) based on PtCo NTA-400 and conventional CCM during accelerated degradation test (right). Reproduced with permission.^[119] Copyright 2017, Elsevier. d) SEM image of as-spun nanofiber. e) High-resolution TEM image of fct-FePt NTs (left). f) Schematic of conventional Pt/C cathode electrode and fct-FePt NT cathode electrode (right). Reproduced with permission.^[122] Copyright 2015, Wiley-VCH GmbH.

in the ORR process. Consequently, the MEA with PtCo NTAs achieves higher Pt utilization by 1.7-fold than the conventional MEA with the Pt/C catalyst. Furthermore, the MEA with PtCo NTAs exhibited enhanced electrochemical durability, and no loss in ECSA was observed after 5000 ADT cycles (Figure 8c). In similar work, ordered intermetallic PtFe NTs was reported by Lee et al.^[122] The SEM and transmission electron microscopy images in Figure 8d,e, show that the PtFe NTs were well constructed by the electrospinning method, and the synthesized face-centered tetragonal (fct)-FePt NTs exhibit an ORR-specific activity that is approximately three times higher than that of commercial Pt/C catalysts. Furthermore, even after the high potential exposure at 1.4 V for 3 h, only 23% of ECSA loss was observed from fct-FePt NTs, whereas Pt/C exhibited a 73% decrease. These enhanced catalytic activity and electrode durability are due to the formation of a well-ordered intermetallic 1D structure and carbon support-free, as well as thin and robust electrode (Figure 8f).

As we examined above, 1D structured electrodes including carbon materials-supported or supportless Pt catalysts have superiority compared to the conventional 2D flat electrode in terms of catalyst utilization and mass transport phenomena

through vertically aligned channels. And, the 1D structured electrodes without supporting materials can have the additional advantage of high electrode durability. However, the manufacturing process of ordered 1D structures includes many steps and is time-consuming and their morphology control such as length, diameter (aspect ratio), and density is very challenging. However, in the case of Pt/VACNT from Toyota's work, although the usage of CNT and ionomer might be undesirable for the MEA durability and the preparation process is complicated, it has exceeded DOE targets and has already been verified for the mass production of large area MEA (236 cm²) and its usability as a product. Therefore, a strong bond between the academe and industry should be required for further developing and validating the lab-scale products and techniques to fit the commercial level.

3.3. 3D Structured Electrode Structures

Different from the structural characteristics of 1D electrodes with vertically aligned channels, interconnected 3D hollow and porous electrode structures that are wide open and have low

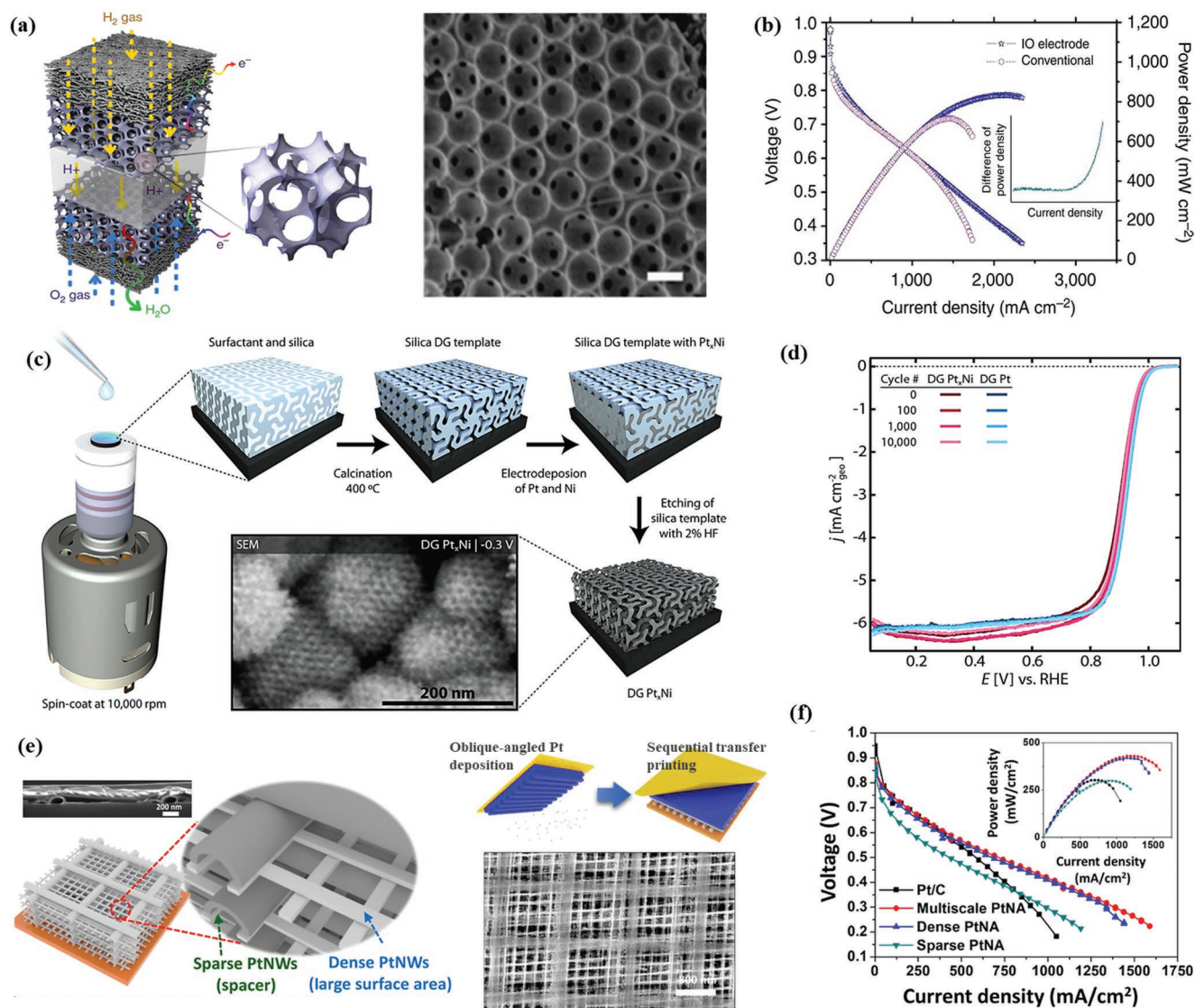


Figure 9. a) Conceptual diagrams of modified MEA with IO electrode and SEM image of IO electrode surface (scale bar: 500 nm). b) Polarization curves of IO electrode-based MEAs (0.12 mg cm^{-2} at 80°C) and supply of 1.5-bar pressurized and fully humidified H_2/air . Reproduced with permission.^[126] Copyright 2013, Springer Nature. c) Synthesis procedure and structural model for mesoporous DG PtNi alloy; SEM image showing interlocked and twisted network structure of DG PtNi; the same synthesis procedure was used for DG Pt. d) Initial and post potential cycling ORR polarization curves for DG PtNi and DG Pt, respectively. Reproduced with permission.^[127] Copyright 2016, Elsevier. e) Schematic showing multiscale Pt nanoarchitectures (PtNAs) and SEM images of multiscale PtNA electrode. f) Polarization curves of Pt/C and various PtNA-based MEAs in non-pressurized H_2/air at 80°C . Reproduced with permission.^[29] Copyright 2021, American Association for the Advancement of Science.

tortuosity allow the facile access of reactant gas to active sites, as well as secure electronic conductivity and improve durability owing to their connected structure and carbon-free nature.^[115] Kim et al.^[126] constructed ordered 3D macroporous Pt electrodes using an inverse opal (IO) structure, which is periodic and has a large surface area and interconnected macropores (Figure 9a). By dip coating the GDL into a PS ($\approx 500 \text{ nm}$) colloid suspension, multilayered, self-assembled, and closely packed PS sacrificial scaffolds were prepared. Moreover, Pt was deposited on the PS-coated GDL by pulsed electrodeposition where the GDL acted as a working electrode, and the PS scaffold was removed. The fabricated 3D IO structure electrode has a Pt loading amount of 0.12 mg cm^{-2} and thickness of $1.5\text{--}2 \mu\text{m}$.

With this thin electrode, the ionomer was unnecessary, and this interconnected 3D ordered electrode provides the advantages of short diffusion pathway and increased conductivity of reactants and ions. Based on these properties, the performance of the MEA with the IO electrode is better than that of the MEA with the same Pt loading (Figure 9b), indicating the efficacy of the IO electrode in improving mass transport. As other examples on the construction of 3D porous and ordered electrodes with a sacrificial template and the use of a Pt alloy catalyst, Jaramillo et al. reported ordered mesoporous Pt, and PtNi thin-film electrocatalysts with double-gyroid (DG) structures.^[127,128] They employed silica template-assisted Pt and employed Ni electrodeposition, followed by etching (Figure 9c). The diffusivity of

this particular mesostructured DG is an order of magnitude higher than those of other mesoporous structures, thus enabling the facile transport of gases and water through the structure. In addition, high-surface-area mesostructured Pt and PtNi DG thin-film catalysts exhibit high ORR activity and stability owing to their unique structure with few undercoordinated Pt sites. Undercoordinated Pt sites, such as step, corner, and edge sites, are presumed to be less active for the ORR than the atoms on flat planes due to the strong chemisorption toward oxygen species during ORR. Moreover, they are associated with ORR activity loss. Even after 10 000 cycles of accelerated durability test, DG Pt maintained more than 80% of the initial ECSA, and only 7 mV of degradation in the half-wave potential was observed. In the case of DG Pt_xNi catalysts, 82% of their initial ECSA values were maintained and showed a virtually unchanged ORR specific activity (Figure 9d). Unfortunately, only half-cell results have been reported for both the DG Pt and PtNi catalysts. As mentioned above, actually there may be differences between single-cell and half-cell tests, single-cell measurement of their developed catalyst is highly required for verifying their superiority compared to conventional catalysts.

As a multiscale approach in 3D electrodes by the combination of electrodes with different structural shapes and dimensions, recently, Kim et al. developed a multiscale multilevel 3D orthogonal grid-patterned electrodes without the use of 3D scaffolds for the nano-transfer printing of individual Pt nanowire building blocks (Figure 9e).^[29] The 3D electrode composed of multiple layers of 2D patterns with different line patterns (pitch/width of 200 nm/50 nm and 1.2 μm/200 nm) was prepared. The successive fabrication processes are as follows: 1) Fabrication of silicon masters with different patterns. 2) Replication pattern from the masters. 3) Obliquely deposition of Pt on the patterned substrate. 4) Repeated transfer of 2D-arrayed Pt nanopattern to the substrate. 5) Thermal annealing process for obtaining a polycrystalline Pt nanostructure. 6) Transferring the 3D electrode to the membrane surface. The MEA with the multiscale 3D Pt electrodes exhibited 43% higher maximum power density (430 mW cm⁻²) than the conventional Pt/C electrode using the same Pt loading amount of 0.08 mg cm⁻² (Figure 9f). In particular, the improved performance was remarkably represented in regions with high current density where mass transfer losses were dominant. This was because the combined architecture electrode facilitated the mass transfer through the open path while securing sufficient active sites. The electrode consisted of a dense and narrow (pitch/width of 200 nm/50 nm) part adjacent to the membrane side and a sparse and broad (pitch/width of 1.2 μm/200 nm) part adjacent to the GDL side. Moreover, the ADT for 5000 cycles revealed that the carbon-free 3D Pt electrode exhibits improved electrode durability with a marginal loss in initial ECSA (5%), which is a considerable improvement compared with the 69% loss in Pt/C electrode.

The 3D structured electrodes showed great potential to reduce particularly mass transfer resistance from the advantage of interconnected 3D hollow and porous electrode structures. And, the durability issues were largely alleviated by their carbon-free nature. Compared to 1D structures including tube, wire, or fiber, 3D structured electrodes showed a much higher degree of freedom in designing their morphologies as shown

above including IO, or multiscale scaffolds. In addition, 3D structures have higher structural stability compared to 1D structures having technical issues during the MEA fabrication processes such as collapse or transfer of the structures (bundling, fracture) due to their high aspect ratio characteristic as represented in Toyota's work.^[30] Despite several structural advantages of 3D structured electrodes, applying the electrodes has a long way to go due to the complicated manufacturing process, low yield, and difficulties in scale-up.

3.4. Summary of Electrode Modification

We categorized previous research on electrode modification for improving the utilization of the catalyst and mass transfer, consequently lowering $\eta_{kinetic}$ and η_{mass} , respectively, into three topics of pore-control and 1D and 3D structured electrodes, and their performances are summarized in **Table 2**. While the MEAs with pore-controlled electrodes showed improved performances compared to conventional Pt/C electrodes by about 20–30%, significantly improved peak power densities (more than doubled) were observed in the MEAs with 1D and 3D structured electrodes with extremely low platinum loading (minimum 3.5 μg cm⁻²). This is ascribed to the optimization of electrode structure together with advanced materials approaches (e.g., Pt alloy catalysts), and this led to maximized Pt utilization and minimized mass transport resistances. In addition, catalysts and carbon-support durability issues were extremely alleviated in the case of the well-designed and supportless 1D and 3D electrodes. However, it can be said that the development of a new catalyst for constructing 1D and 3D electrodes has much more limitations in terms of process difficulty, complexity, and scale-up ability compared to the pore-controlling strategies using commercial Pt/C catalysts and pore-formers. Therefore, it is necessary to develop electrode manufacturing techniques with high feasibility and reproducibility that can be used in the industrial field.

4. Transport Layer Engineering Approach

The water generated from the ORR on the cathode side, which induces concentration loss by blocking the catalyst surface must be properly removed from the electrode to generate electricity because fuel and oxidant gases must be continuously supplied to the electrode and approach to TPBs. The transport layers corresponding to the GDL and flow channel play a critical role in mass transport and device performance. The mass transport in the fuel cell is dominated by convection in the macroscale flow channels and diffusion in the microscale pores in the GDL.^[2,39] Hence, an appropriate design for flow channel configuration and pore distribution in the GDL based on understanding the dynamic fluid behavior is crucial to the enhancement of the gas transport from the flow channel to the electrode. In addition, controlling the wettability of pore structures is also important for effective water management in the fuel cell system to reduce concentration loss. In view of the foregoing, the structural design and modification of GDL and flow channels to facilitate mass transport are presented in this section.

Table 2. Diverse electrode modification strategies and their effects on PEMFC performance.

Type	Feature	Main Improvement	Mass-norm. Power [W mg ⁻¹ _{Pt}]	Max. Power [Imp.] [mW cm ⁻² [%]]	Cathode Pt [mg cm ⁻²]	Operating Environment	Note	Ref.
Pore-control								
	PS for pore fabrication	Pt utilization (0.23 mg W ⁻¹) was tripled	4.35 @ 0.6 V	200 (33) ^{a)}	0.047	H ₂ /Air, RH 80/100 (100 kPa), 60 °C	PS 70 wt% PS diameter: 0.5 μm	[112]
Spraying	MgO for pore fabrication	Effective oxygen diffusivity was doubled (11.6 × 10 ⁻⁴ cm ² s ⁻¹)	5.92 @ 0.5 V	592 (36) ^{c)}	0.08	H ₂ /Air, RH 100 (150 kPa), 80 °C	Dual-layer electrode	[113]
Stretching	Stretching for crack	14% lower Ohmic resistance, 43% lower Warburg impedance	3.60 @ 0.45 V	720 (22) ^{d)}	0.2	H ₂ /Air, 100% RH, 70 °C	Strain: 1.5	[31]
Imprinting, Stretching	Prism-pattern. Memb. Stretching for crack	78.8% lower Warburg impedance (0.6 V)	4.33 @ 0.5 V	863 (18) ^{c)}	0.3	H ₂ /Air, 100% RH, 70 °C	Pattern pitch: 20 μm, Strain: 0.5	[24]
1D and 3D structured								
Spraying	3D macroporous Nafion nano-composite electrode	31% higher maximum power density, 9.5% higher ECSA (86.35 m ² g ⁻¹)	3.82 @ 0.5 V	955 (31) ^{c)}	0.25	H ₂ /Air, RH 100 80 °C	Nafion/ Cs _{2.5} H _{0.5} PW ₁₂ O ₄₀ scaffold (10% CsHPW)	[115]
Galvanic displacement	PdCo NT with thin Pt array (Pt _{skin} @ PdCo NTAs)	13.7-fold higher PGM-norm. power density, 13% ^{initial} , 82% ^{e)} larger ECSA	21.70 @ 0.6 V	493 (247) ^{c,e)}	0.0035	H ₂ /O ₂ , RH 100 (200 kPa), 80 °C	Ultrathin Pt skin on open-walled PdCo nanotube arrays	[116]
CVD, Decal transfer	Electrode based on VACNTs	2.6 A cm ⁻² at 0.6 V with extremely low Pt loading, large-area (236 cm ²)	10.40 @ 0.6 V	1560 (30 ^{f)}) ^{a)}	0.1	H ₂ /Air (150/100 kPa), Anode dew point 45 °C/Cathode dry, 65 °C	VACNTs: length = 40–60 μm, diameter = 20 nm, average distance = 200 nm,	[30]
Magnetron sputtering, Decal transfer	Open-walled PtCo bimetallic NTAs	1.7-fold improvement in Pt utilization; no loss in ECSA after ADT	14.38 @ 0.5 V	758 (134 ^{e)})	0.0527	H ₂ /O ₂ , RH 80 (200 kPa), 80 °C	Open-walled PtCo bimetallic NTAs with length of ≈3 μm and diameter of ≈100 nm	[119]
Electrospinning, Sputtering, Decal transfer	PVA nanofiber templates	92% higher power density; ^{e)} 35% lower charge transfer resistance ^{e)}	22.25 @ 0.6 V	935 (7) ^{c)}	0.042	H ₂ /O ₂ , RH 100 (200 kPa), 80 °C	Diameter of Pt-coated PVA nanofibers: 185 nm	[121]
Electrospinning, Spraying	fcc-FePt NTs prepared by co-axial electrospinning	Only 10% degradation rate at 0.7 V and 23% loss in ECSA after ADT at 1.4 V	5.65 @ 0.4 V	399.6 ^{b)} (234 ^{e)})	0.2	H ₂ /Air, 100% RH (150 kPa), 80 °C	Support-free intermetallic fcc-FePt NTs	[122]
Polyol synthesis Pulsed spraying	Connected Pt–Fe catalysts via silica template and by etching	No loss in ECSA after 10 000 cycles of ADT	N/A	N/A	0.32	H ₂ /O ₂ , RH 90/70, 80 °C	Pore size: ≈10 nm, Outer diameter: ≈400 nm	[129]
Electrodeposition	IO structure electrode (IO Pt)	185% higher current density at 0.6 V, 136% larger ECSA	6.97 @ 0.4 V	836 (17) ^{c)}	0.12	H ₂ /Air, RH 100 (150 kPa), 80 °C	Mean diameter of PS particles: 520 nm	[126]
Photolithography Nano-transfer	3D structure composed of multiple 2D lines of different sizes (multiscale PtNA)	18.1% peak power density loss from multiscale PtNA ^{e)} (72.5% loss in Pt/C ^{e)})	5.38 @ 0.4 V	430 (43) ^{c)}	0.08	H ₂ /Air, RH100 (100 kPa), 80 °C	Line pitch/width: 50 nm/20 nm, 200 nm/50 nm, and 1.2 μm/200 nm	[29]

^{a)}Value based on 0.6 V current density; ^{b)}Value based on 0.4 V current density; ^{c)}Peak value; ^{d)}Estimated value from graph/paper; ^{e)}ADTs; ^{f)}Comparison with US DOE 2017 target specific power per PGM mass (kWg_{PGM}⁻¹).

4.1. Structurally Designed GDL

The material used in GDLs should be electrically conductive and chemically resistant, and the porous network should be electrically well-connected for electron transfer from anode to cathode. Hence, carbon-based fibers and particles are generally used to construct GDLs. Conventional GDLs consist of carbon paper with hundreds of micrometer-sized fiber networks in contact with the flow channel. Moreover, a microporous layer (MPL) composed of aggregate of nanosized carbon particles is in contact with the electrode to uniformly supply fuel or oxidant gas while minimizing contact resistance at the interface. Based on this structural morphology, a certain amount of hydrophobic polytetrafluoroethylene (PTFE) binder was incorporated into the GDL to alleviate water flooding, which severely blocks the gas supplied to the porous layers.^[130,131] In the case of commercially manufactured GDL, the thickness of the carbon paper/MPL and PTFE content are adjusted depending on the target operating conditions.^[132–134] However, the homogeneous through-plane morphology of the carbon materials in each MPL and carbon paper layer can limit the transport efficiency based on the fact that the optimized structure would force the liquid water to move efficiently from the electrode side to the flow channel side by inducing structural driving force in through-plane direction. In addition, liquid water and reactant gas are transported through the shared pathway in the GDL because of the homogeneously distributed PTFE and carbon network morphology that both restrict the mass transport efficiency.^[135,136] Based on these transport problems, architecting strategies, including PG, micro-hole perforation, and patterned wettability technologies, have been applied to the GDL to improve mass transport (Figure 10a). The key strategy of the novel approaches is inducing a favorable moving direction for liquid water through the non-homogeneous/gradient structure and wettability design, which leads to enhanced water transport toward the outside and separating the liquid water pathway from the gas phase reactant pathway.

The generated water droplet was drained through the porous GDL structures induced by the pressure difference. This behavior can be explained by the Young–Laplace equation, as follows:^[144,145]

$$P = -\frac{2\gamma\cos(\theta)}{r} \quad (6)$$

In this equation, the threshold pressure, P (also referred to as the breakthrough pressure), is determined by the pore radius (r), contact angle between a liquid droplet and GDL surface (θ), and surface tension of water (γ). Based on this relationship, with respect to pore geometry, a gradually increasing pore size distribution from the electrode side to the flow channel side through the GDL was more advantageous to water discharge. However, because the conventional GDL has a homogeneous pore distribution in each MPL and carbon paper layer, a GDL with a PG has been developed to enhance the water transport to the flow channel. This type of GDL contains coarse structures in the face in contact with the flow channel and a dense structure in the face in contact with the electrode. Oh et al. constructed GDL substrates with a pore size gradient by arranging a dual-layered

carbon fiber substrate with fiber lengths of 13 and 6 mm.^[135] The performance of a single cell with PG GDL compared with a no-PG (NPG) GDL cell is better under 50% and 100% RH operating conditions. The single cell with PG compared with that with NPG showed 2.69% higher performance at a low current density of 0.4 A cm⁻² under the 50% RH condition as well as 15.30% and 22.20% improved performance at a high current density of 1.6 A cm⁻² at 50% and 100% RH, respectively. Based on the transient response, voltage instability test, and EIS, the Ohmic resistance of the PG case was confirmed to be reduced by the improved hydration of the membrane under low current density and RH conditions. Moreover, the decrease in the overall resistance of the PG sample in the region with high current density (regardless of the RH condition) was attributed to the reduced kinetic or mass transport resistance rather than the reduced Ohmic resistance. The results indicate that the small pores in the first carbon substrate facing the electrode reduce the capillary pressure gradient from the MEA to the GDL. In turn, the back diffusion of water toward the MEA is enhanced. Therefore, the PG structures in the GDL can result in a smooth supply of reactant gases toward the electrode with a sufficiently hydrated membrane under low RH conditions. The large macropores facing the flow channel in the second substrate increase the capillary pressure gradient from the MPL to the flow channel, facilitating the drainage of water that accumulated in the GDL toward the channel. Consequently, mass transport is promoted through effective water management in high current density regions and under high RH conditions.

To investigate the effect of the degree of PG, Ko et al. prepared three GDLs with NPG and medium and high PGs having a comparable average porosity (≈ 0.82); they operated the single cells under 25% and 100% RH conditions (Figure 10b).^[137] Interestingly, the GDL type exhibiting the highest performance varied depending on the RH condition. Under low RH conditions, the medium PG GDL exhibited the best performance, whereas the high PG GDL exhibited reduced performance. The low performance of the latter was induced by the reduced liquid water saturation and dehydration of the membrane due to the high water removal capability of the high PG GDL, as confirmed by in situ X-ray visualization. However, this capability leads to the highest performance under the 100% RH condition, indicating that the extent of the PG must be carefully considered according to the operating conditions.

Although GDLs with an increased pore size gradient from the electrode interface to the flow field interface exhibit improved performance due to their excellent water removal capacity, the construction of fine-tuned gradients to obtain optimal water balance remains a challenge. This is because of the complexity of the conventional process in manufacturing GDLs with controlled pore size gradients. To resolve this problem, a simple electrospinning manufacturing process for fabricating GDLs with controlled pore size gradients was introduced (Figure 10c).^[138] By applying high voltage to a viscous polyacrylonitrile (PAN) droplet, an ultrafine fibrous polymer substrate was constructed on the ground surface. After the carbonization process of the two-step heat treatment, the polymer substrate was converted into carbon fibers. Balakrishnan et al. fabricated bi- and single-layered GDLs with fiber diameters of 174 and 687 nm as well as pore diameters of 190 and 690 nm.

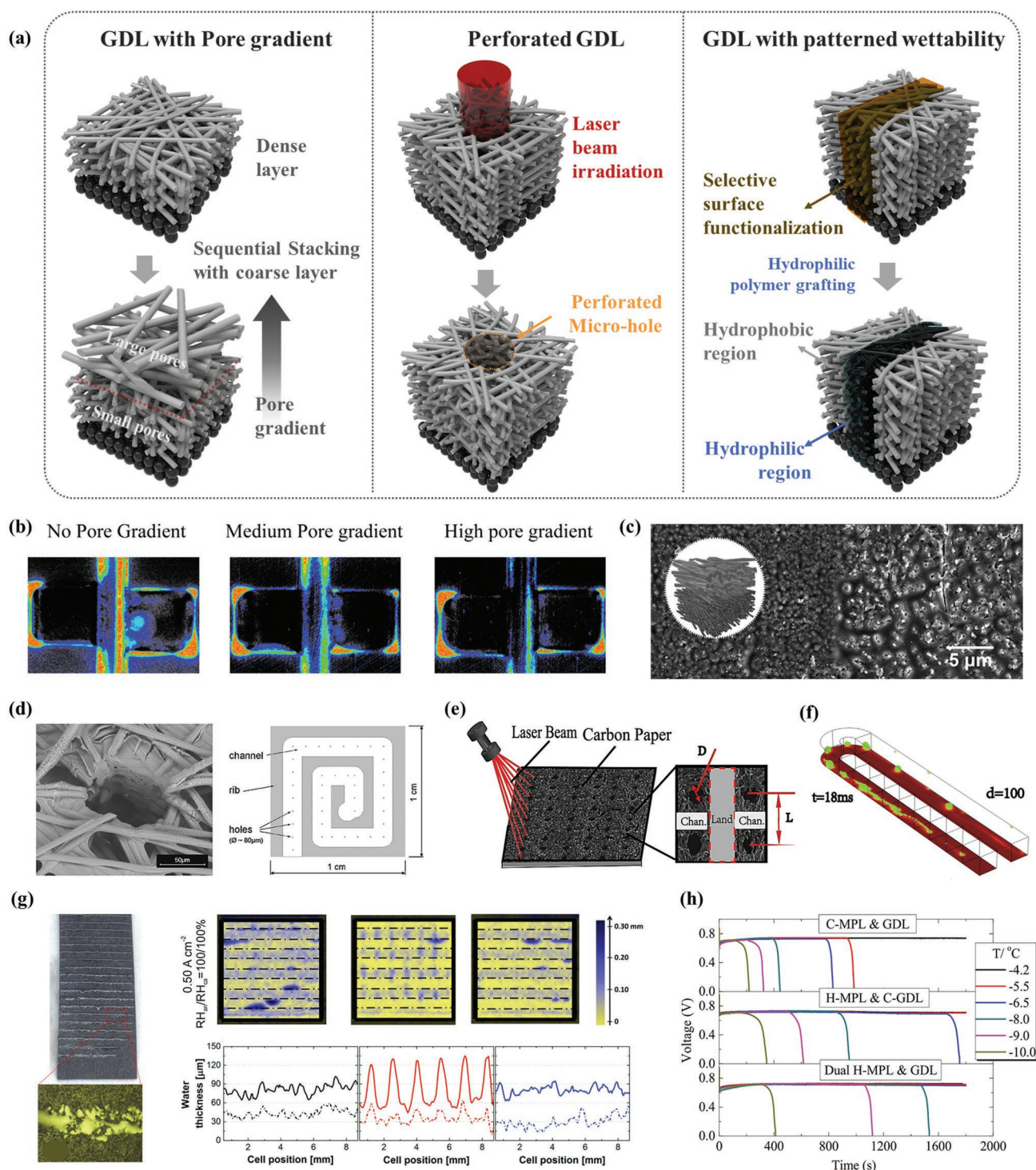


Figure 10. a) Overview and simple fabrication schemes of structurally designed GDL: GDL with PG from electrode facet to flow field facet; perforated GDL containing micro-hole array; and GDL with patterned wettability, which is divided into hydrophobic and hydrophilic regions. b) X-ray visualization image at 100% RH and current density of 1.0 A cm⁻² of GDL with no/medium/high PG; color indicates the amount of water. Reproduced with permission.^[137] Copyright 2018, Elsevier. c) SEM images and pore size distributions of tailored GDLs with 8 and 12 wt% PAN solution. Adapted with permission.^[138] Copyright 2020, American Chemical Society. d) SEM image and schematic of 80-μm hole arrays burnt into GDL by laser beam. Reproduced with permission.^[139] Copyright 2008, Elsevier. e) Schematic and SEM images of perforated carbon paper having different penetration hole diameters with laser perforations. Reproduced with permission.^[140] Copyright 2017, Elsevier. f) Simulation result of the droplet transfer process of perforated GDL. Reproduced with permission.^[140] Copyright 2017, Elsevier. g) Water accumulation in hydrophilic patterns and magnified optical microscope image of water accumulation on the hydrophilic pattern (left). Reproduced with permission.^[141] Copyright 2016, ECS. Through-plane neutron radiographs for three cells (without MPL) containing different cathodic GDLs at 0.50 A cm⁻² and corresponding water profiles at the bottom (right). Reproduced with permission.^[142] Copyright 2016, ECS. h) Variation in voltage of PEMFC with different structures of hybrid MPL/GDL with patterned wettability. Reproduced with permission.^[143] Copyright 2020, MDPI.

Electrochemical measurements confirmed that the bi-layered GDL exhibited a lower mass transport loss than the single-layered GDL, indicating effective water removal and oxygen diffusion. The remarkable improvement in the performance of the bi-layered GDL (0.86 W cm^{-2}) by a 131% higher peak power density compared with that of the commercial GDL (Toray, TGP-H-060 GDL) was reported.

The graded pore structure in the carbon papers and the large pores in the dense MPL can be effective for improving mass transport. After forming an MPL with a mixture of pore former and carbon nanoparticles, the pore former was selectively dissolved using an organic solvent.^[146,147] The single cell with the GDL with hierarchical pores showed peak power densities of 1.22 and 1.24 W cm^{-2} at 60% and 100% RH, which are 20.1% and 78% higher than those of the commercial one, respectively. Furthermore, diverse experiments with different pore distributions caused by changing the pore former concentration in the carbon ink were conducted. The authors found that increasing the pore size in the range of 7–20 and 20–100 μm in the hierarchical pores included in the GDL is effective in facilitating the water and gas transport in PEMFCs.

Another approach for modifying the MPL to improve water management was the introduction of an MPL with spatially graded PTFE.^[136] This novel MPL was fabricated with a spatial gradient of the PTFE content, which decreased in concentration from the electrode side (20 wt%) to the carbon paper substrate side (10 wt%). In contrast, the reference MPLs contained constant PTFE concentrations of 10 and 20 wt%. Measurements confirmed that performance improvement was insignificant at relatively low current densities ($<1.0 \text{ A cm}^{-2}$). However, at high current densities ($>1.0 \text{ A cm}^{-2}$), the performance improvement was evident because the water accumulation in the GDL was alleviated, as verified by synchrotron X-ray radiography. In particular, the mass transport resistance of the fuel cell with the 20% PTFE MPL significantly increased by 440% when the current density range was 1.0–1.5 A cm^{-2} , whereas the single cell with graded PTFE in the MPL only exhibited a 72% increment. This improvement was attributed to the increased pore size and wettability of the PTFE-graded MPL toward the side of the carbon paper, reducing the threshold capillary pressure and enhancing the capillary-driven removal of liquid water.

Based on the same PG strategy, the periodic microscale perforation to the GDL is one of the strategies for improving mass transport. Lu et al. reported that a perforated GDL facilitated water management and uniform liquid water distribution in the MEA.^[148] The authors modified the GDL using a laser perforation technique to engineer holes with controlled sizes and patterns. The perforation pattern was a square-shaped array comprising 100- μm -diameter holes spaced at 1 mm; the foregoing was used only in the MPL. A single cell with perforated GDL exhibited high performance under 90 °C/30% RH and 40 °C/100% RH conditions. To elucidate the effect of perforation, neutron imaging of ex situ water transport was conducted. In the reference cell, the water thickness was found to fluctuate in the range 0.2–1.3 mm, whereas that in the cell with the perforated GDL remained relatively uniform. Moreover, the breakthrough pressures were confirmed to be 25.0 and 9.5 kPa for the reference and perforated GDLs, respectively. The foregoing was confirmed through an ex situ water transport experiment,

which indicated that the local perforation of the MPL was effective in achieving uniform water distribution and better water transport in the GDL. Gerteisen et al. perforated the carbon paper (instead of the MPL) with 80- μm -diameter holes (1 mm apart) and observed performance improvement (Figure 10d).^[139] In the case of the perforated GDL, the limiting current density increased by 22% compared with that of the pristine GDL. By chronoamperometry measurement, which shows the transient current response to rapid voltage step changes, overshoot and undershoot behaviors are observed in the case of pristine GDL. In contrast, an extremely small overshoot in the perforated GDL is recorded. The results indicate that the large fabricated pores act as water transport channels for capillary diffusion, leading to facile water distribution without requiring high-pressure gradients and a reduction in the saturation level on the cathode side. The reduced water accumulation and minimized oxygen diffusion resulted in improved dynamic and overall fuel cell performance.

To investigate the size effect of the perforated holes in the GDL, Wang et al. fabricated holes using a laser. The hole diameters are in the range 80–200 μm and spaced 1–3 mm on centers (Figure 10e).^[140] In terms of the effect of hole size on performance and water distribution, a single cell in which the GDL is perforated with a 100- μm -diameter hole exhibited the best performance ($851.52 \text{ mW cm}^{-2}$) in the experimental set of hole diameters (80, 100, 160, and 200 μm with the same 1-mm spacing), and this is also confirmed through simulation study of droplet transfer process of perforated GDL (Figure 10f). As for the influence of perforation spacing on performance, a single cell with a perforated GDL in which the holes are spaced 2 mm apart exhibited superior performance compared with the GDLs with holes that are 1 and 3 mm apart. Based on the experimental and simulation results, the authors found that the optimal perforation size and spacing were 100 μm and 2 mm, respectively. In each case, when the water droplet generation and removal process are considered, the droplets emerge from the pores, grow, and then split; then, they are removed through the channel. When the pore size is less than 100 μm , a high-pressure gradient is required to transport water through the hole in the GDL such that water can cover the surface of the catalyst and fill the gaps at the interface. However, in the case of large pores exceeding 100 μm in diameter and narrowly spaced at less than 1 mm, blowing away the emerging droplet was difficult. Consequently, the droplets merge into larger slugs that clog the channel, indicating the importance of cautiously selecting hole dimensions.

Because perforating the GDL has been demonstrated as an effective method for improving mass transport in fuel cells, this technique has recently been used to develop ultrathin, flexible, and high-performance GDLs. Wei et al. developed a novel type of GDL to overcome the problems encountered in the fabrication of commercial GDLs (e.g., complex preparation processes, extremely high preparation temperature [2000 °C], and considerable thickness). The fabrication process mainly consists of three steps: drilling of pore array with a diameter of $\approx 50 \mu\text{m}$ on CNT films; coating of MPL with a mixture of CNT and PTFE; and heat treatment at 350 °C.^[149] The thickness of this novel GDL is 40 μm , which is only $\approx 15\%$ of that of commercial GDLs. Moreover, with a minimum bending radius of less

than 0.17 mm, this GDL is highly flexible. With the developed GDL, the geometrical features were not only advantageous but the device performance was also remarkable. The single cell with the developed GDL exhibited a maximum power density of 840 mW cm⁻², which was 32.5% higher than that of commercial GDLs, owing to the improved mass transport. Based on this estimate, if the conventional GDLs in the stack system were replaced by the novel GDLs, the stack volume could be reduced by 19.3%, greatly improving the volume-specific power density by 64.2%.

Thus far, the mechanical and structural strategies for modifying the GDL to enhance mass transport have been identified. Another scheme for enhancing mass transport without modifying the structures is a patterned wettability strategy that separates the water and reactant gas pathways. It is based on the fact that GDLs contain a random porous network with carbon fibers and particles and that the transport pathways for reactant gas and liquid water are shared. Forner-Cuenca et al. conducted a comprehensive study on patterned wettability tuning by functionalizing the hydrophilic polymers to GDLs for the operando characterization of water distribution in fuel cells (Figure 10g).^[142,150] First, the hydrophilic functionalization of the GDL surface was achieved by e-beam activation and polymerization reactions. The MeV electron activation process was found effective in producing radicals throughout the material thickness. Subsequently, two types of hydrophilic polymers, acrylic acid (AA) and N-vinylformamide (NVF), were grafted onto fluorinated ethylene propylene that was previously coated on the GDL as a hydrophobic material for commercial use. Hydrophilic functionalization was successful unless the polymer coating load was less than 5–30 wt% relative to carbon weight, which depends on the materials. The functionalized GDL was not sintered at 270 °C, which induces the decomposition of grafted polymers. Radiation-blocking steel masks with widths and spaces of hundreds of micrometers were used to realize line-patterned wettability. With this fabrication strategy, the hydrophilic and hydrophobic domains were separated, as confirmed by the water imbibition experiment. The NVF-treated GDL exhibited better-defined hydrophilic and hydrophobic domains than the AA-treated GDL. Based on these findings, they conducted an in situ characterization of a fuel cell with a GDL with patterned wettability. Polarization curve measurements were combined with pulsed gas analysis, enabling the evaluation of mass transport losses. Neutron radiography was simultaneously performed to capture an image of the water distribution during cell operation. The results indicated that the generated water tended to accumulate preferentially under the rib areas on the cathode side. The cell with the conventional GDL contained higher amounts of water under the channel areas than the cells with patterned GDLs. This is because the hydrophilic regions attract the distributed water from the hydrophobic domains, leading to the removal of the dense water layer. This water segregation resulted in increased oxygen diffusivity through the hydrophobic region. This was confirmed by the increased power density and reduced bulk losses in the case of cells with GDLs that have patterned wettability.

In addition to the improvement under normal operating conditions, the GDL with patterned wettability exhibited excellent cold-start performance, which was a critical problem among

commercial fuel cells. The MPL and GDL substrates with patterned wettability in which hydrophilic and hydrophobic lines were arranged alternately with a stripe width of 1 mm in the in-plane direction were fabricated. This hybrid dual GDL showed a better cold-start ability than the conventional GDL (Figure 10h).^[143] The fuel cell with the dual hybrid GDL operated for more than 30 min at –5.5 and –6.5 °C, whereas the conventional GDL operated for less than 17 min at less than –5.5 °C. In particular, the operation time of the fuel cell with the dual hybrid GDL was 3.45 and 1.89 times greater than that of the conventional GDL. The results were attributed to the tendency of generated water to stagnate in the gap between the electrode and MPL owing to the hydrophobic properties of the conventional GDL. In contrast, the supercooled water was easily transported and rapidly absorbed into the hydrophilic area of the hybrid GDL before freezing, thus facilitating the gas transport through the hydrophobic area and prolonging the fuel cell operating time.

As previously discussed, architected GDLs with PG, patterned wettability, and micro-hole perforation enable the effective removal of water from the transport layer and facilitate mass transport. The features, conditions, and effects of each strategy are summarized in **Table 3**.

4.2. Flow Field Modification

As one of the key components of fuel cells, the conventional flow channel carved on a bipolar plate generally consists of tens or hundreds of fine grooves. These grooves distribute the reactant gas to the electrode through the GDL and remove the generated water outside the fuel cell. The flow channel design for improving the water management and uniform reactant gas distribution into the electrode is one of the significant factors for enhancing mass transport and device performance. Accordingly, over the decades, considerable efforts to minimize concentration loss have been devoted to developing optimized flow channels. Conventional flow channel configurations, including a single serpentine flow field, Z-parallel or single-parallel flow field, and interdigitated flow field, have been investigated.^[151–153] Although serpentine flow channels are commonly used in PEMFCs owing to their excellent water removal capability, the single pathway of the serpentine configuration leads to a comparatively high-pressure drop.^[153] Moreover, the uniform reactant distribution into the electrode is limited owing to the existence of millimeter-sized ribs between flow channels, which contact GDL for electron transport. In addition, in conventional flow channels, convection is dominant from the inlet to the outlet through the flow channel direction, while the gas should be transported and diffused in the perpendicular direction to the mainstream flow direction. And the fluid flow is laminar which restricts the gas transport to the GDL. To overcome these problems including non-uniform gas distribution, high-pressure drop through the channel, non-effective water removal capacity, and limited mass transport to (from) the GDL, novel flow channels have been developed. In this section, bio-inspired flow channel designs, porous media flow fields, and 3D fine mesh for uniform reactant gas distribution, minimizing pressure drop, and improved mass transport will be addressed.

Table 3. Summary of features of structurally designed GDLs and their effect on performance.

Strategy	Features	Membrane	Catalyst loading	Operating condition	Main improvements	Ref.
Pore gradient	Modified with pore former (CaCO ₃) in MPL near carbon paper	N/A	Anode: 0.2 mg _{pt} cm ⁻² , Cathode: 0.3 mg _{pt} cm ⁻²	100% and 60% RH at 80 °C, SR 5, w/o back pressure (BP), O ₂ : 0.02 L min ⁻¹ cm ⁻² , H ₂ : 0.05 L min ⁻¹ cm ⁻²	Maximum power density: 1.24 W cm ⁻² (+7.8%), Limit current density: 3.5 A cm ⁻² (+3.0%)	[146]
	Electrospinning of PAN, 8-wt% and 12-wt% PAN, pore size gradient	Nafion HP	Anode: 0.3 mg _{pt} cm ⁻² , Cathode: 0.3 mg _{pt} cm ⁻²	100% and 50% RH at 60 °C, H ₂ : 1 L min ⁻¹ , Air: 1 L min ⁻¹ , BP: 200 kPa	Maximum power density: 0.86 A cm ⁻² (+131%)	[138]
	20–10-wt% PTFE gradient	Nafion HP	Active area: 0.68 cm ² Anode: 0.3 mg _{pt} cm ⁻² , Cathode: 0.3 mg _{pt} cm ⁻²	100% RH at 60 °C, Hydrogen: 1 L min ⁻¹ , Air: 1 L min ⁻¹	Less water accumulation (–83%), higher cell potential by 0.09 V and power density by 0.14 W cm ⁻² at 1.5 A cm ⁻² compared with 20% PTFE GDL	[136]
Patterned wettability	Pore size gradient (High PG, Medium PG, NPG)	N/A	Active area: 2 cm × 2 cm Anode: 0.2 mg _{pt} cm ⁻² , Cathode: 0.4 mg _{pt} cm ⁻²	100% and 25% RH at 65 °C, Hydrogen: SR 1.5, Air: SR 2.0	17% higher power density of 1.1 A cm ⁻² (medium PG) than NPG	[137]
	Line-patterned low and high PTFE content in GDL	Nafion 211	Active area: 4 cm ² Anode: 0.2 mg _{pt} cm ⁻² , Cathode: 0.4 mg _{pt} cm ⁻²	90%, 70%, and 50% RH at 80 °C, Hydrogen: 2.0 m s ⁻¹ , Air: 6.0 m s ⁻¹	Increased limiting current density by 4.45%	[190]
	Dual MPL and GDL with patterned wettability	Nafion 212	Active area: 25 cm ² Anode: 0.4 mg _{pt} cm ⁻² , Cathode: 0.6 mg _{pt} cm ⁻²	70% and 100% RH at –10 to (–4.2) °C, Hydrogen: 226 sccm, Air: 95 sccm	3.45 and 1.89 times greater operation times compared with that of conventional GDL	[143]
Micro-hole Perforation	Perforated GDL composed of CNT (thickness: 20 μm) with 52-μm hole patterns created by laser drilling	N/A	Anode: 0.5 mg _{pt} cm ⁻² , Cathode: 0.5 mg _{pt} cm ⁻²	100% RH at 80 °C, Hydrogen: 100 mL min ⁻¹ , Air: 200 100 mL min ⁻¹ , BP: 0.2 MPa	Maximum power density: 840 mW cm ⁻² (+32.5%)	[149]
	Laser-perforated GDL, Hole diameter: 80, 100, 160, 200 μm (spacing: 1 mm)	Nafion 211	Active area: 25 cm ² Anode: 0.2 mg _{pt} cm ⁻² , Cathode: 0.45 mg _{pt} cm ⁻²	100% RH at 60 °C, Hydrogen: SR 1.5, Air: SR 5.0	Maximum power density: ≈850 mW cm ⁻² (+13.3%) in case of 100-μm hole with 1-mm spacing	[140]
	Laser-perforated GDL, Hole diameter: 100 μm (spacing: 1 mm)	18-μm-thick membrane	Active area: 5 cm ² Anode: 0.1 mg _{pt} cm ⁻² , Cathode: 0.4 mg _{pt} cm ⁻²	100% RH at 40 °C, 100% RH/30% RH at 90 °C (anode/cathode), H ₂ : 0.21 slpm, Air: 1.24 slpm	Breakthrough pressures: 9.5 kPa for perforated GDL and 25.0 kPa for reference GDL, 2 A cm ⁻² at 0.2 V (+53.8%)	[148]

Bio-inspired designs have been extensively applied to achieve optimal flow channels that exhibit pressure drop reduction, uniform reactant gas distribution, and effective water drainage capacity. For example, Kloess et al. introduced a 2D flow channel with leaf and lung designs (Figure 11a).^[154] In plants, water and nutrients are transported through the main vein to many small branches. In the lungs, oxygen and carbon dioxide are exchanged in the bronchus through many interconnected bronchioles. Inspired by these transport functions, novel flow channel designs have been devised. The simulation and experimental results of flow channels whose designs are based on the leaf and lung exhibited a noticeable reduction in pressure loss by up to 37.4% and improved performance by up to 30% in peak power density owing to the uniform reactant gas distribution and convective flow. In addition, the optimal operating conditions when applying these novel-designed flow channels were

found to be ≈70 °C of cell temperature, 2 atm of back-pressure, and 100% RH. In addition to the bio-inspired optimal design in the in-plane direction, a channel design in the through-plane direction was introduced to facilitate the vertical mass transport to the GDL and MEA. Cai et al. developed a wave-like channel inspired by cuttlefish fins with conical-shaped and convexly protruding features (Figure 11b).^[155] This 3D wave-like channel (including straight bumps across the channel) compared with the conventional wave-like channel reserved the flow area on the two edge sides of the channel such that the pressure drop was significantly reduced. The optimal design (center amplitude: 0.305 mm; number of wave cycles: 3.52), obtained through the simulation study, yielded a power density (at 0.45 V) that is 2.2% higher than that of the straight channel.

An advanced 3D channel design inspired by the lung architecture was also employed. Trogadas et al. proposed

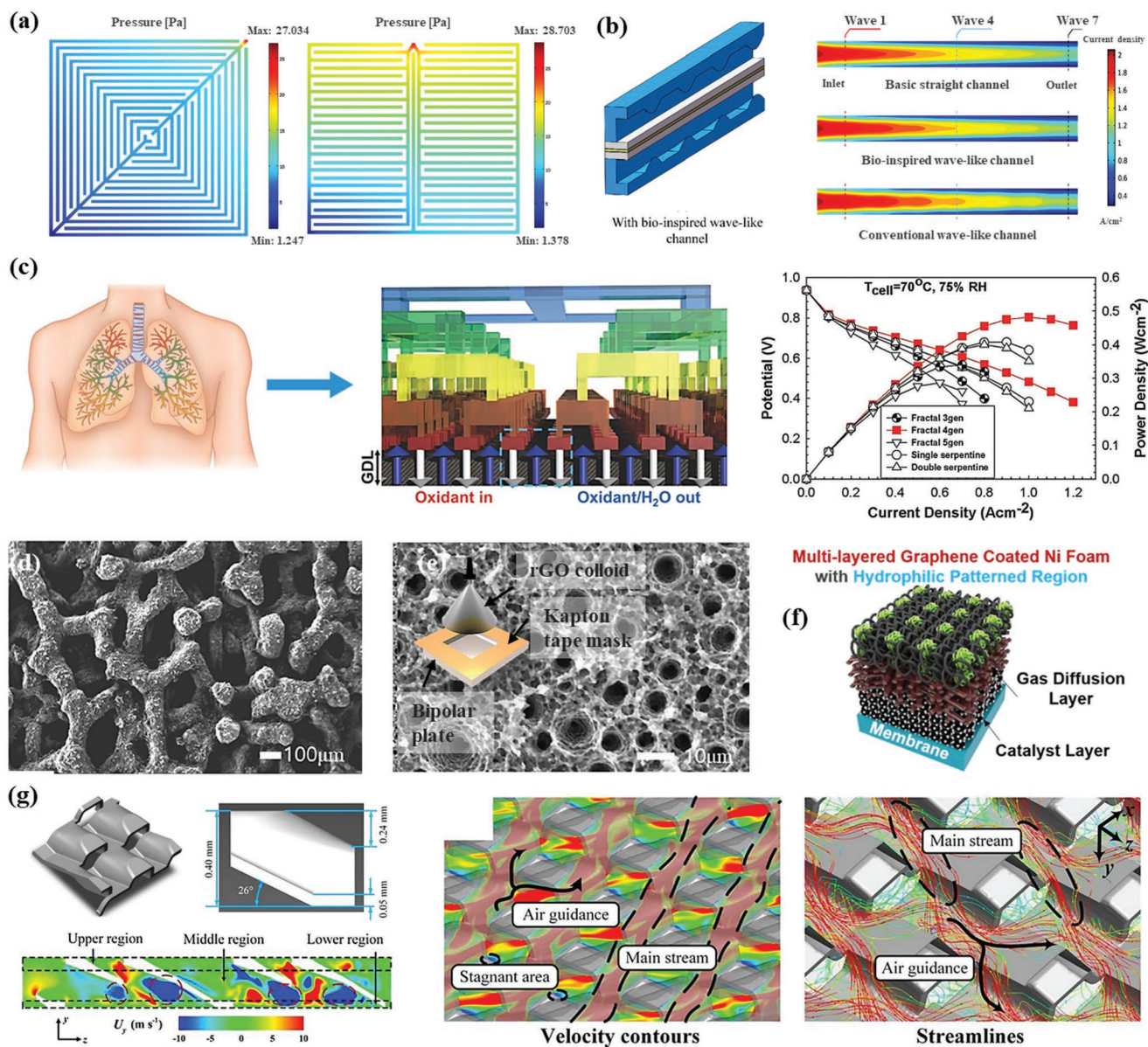


Figure 11. a) Pressure distribution in leaf flow and lung flow patterns. Reproduced with permission.^[154] Copyright 2009, Elsevier. b) Computational domain of PEMFCs with different channels (straight and conventional/bio-inspired wave-like channels) and pressure distribution in each channel. Reproduced with permission.^[155] Copyright 2020, Elsevier. c) Design of lung-inspired flow fields for PEMFCs (left). Improved performance ($N = 4$) compared with conventional serpentine flow field-based PEMFCs with 10-cm² flow field area. Reproduced with permission.^[36] Copyright 2018, Royal Society of Chemistry. d) SEM images of graphene-coated Ni-Cr foam. Reproduced with permission.^[156] Copyright 2020, Elsevier. e) SEM images and fabrication scheme of STG. Reproduced with permission.^[156] Copyright 2020, Elsevier. Reproduced with permission.^[157] Copyright 2021, Elsevier. f) Schematic of MLG-coated Ni foam with patterned wettability. Adapted with permission.^[158] Copyright 2019, American Chemical Society. g) Morphology reconstruction of 3D fine mesh flow field (left); single-phase flow pattern (velocity contours and streamlines) of middle and lower regions of 3D fine mesh flow field (right). Reproduced with permission.^[37] Copyright 2019, Elsevier.

fractal-based structures with repeated branching channels in the through-plane direction (Figure 11c).^[36] According to Murray's law, fractal geometry indicates that the cube of the diameter of the parent channel is equal to the sum of the cubes of the diameters of the daughter channels at each level of bifurcation; this repetitive structure can minimize energy losses. The high-level branched channel structures under high-humidity operating conditions showed insufficient convective liquid water

removal capacity owing to the reduced airflow rate within the fractal channel. In contrast, the four-level fractal flow field of the PEMFC exhibited an $\approx 30\%$ increase in power density under 50% and 75% RH conditions. Further, it showed a 50% lower pressure drop compared with the conventional serpentine channels, reducing the energy requirement for pressurizing the reactants.

As mentioned, advanced designs based on channel/rib structures have been employed to improve the mass transport.

However, the uneven distribution of the reactant and limited mass transport remain inevitable owing to the existence of the ribs. This is because the local liquid water that accumulates under the ribs considerably hinders the mass transport in the GDL. To overcome these drawbacks, some researchers have proposed the use of 3D porous structures as flow fields. Porous media with metal/alloy materials with high porosity (>90%), including Ni, Al, and Cu foams, were used to replace conventional flow fields.^[158,159] Although the metal foam-based flow channel successfully improved the fuel cell performance by reducing the dead zone owing to the contact between the rib and GDL, the chemical corrosion problem limits its practical application. In this regard, carbon-based foams, such as graphite and graphene foams, which have satisfactory corrosion resistance and hydrophobicity, have been proposed.^[160,161] However, the relatively weak mechanical strength of carbon-based foam structures hinders their practical use.^[162] To obtain high corrosion resistance while maintaining the high mechanical strength of the metal foam structure, the foam structure was graphene-coated by chemical vapor deposition (CVD).^[162] Recently, the direct coating of reduced graphene oxide (rGO) on the Ni–Cr foam through the superheat vaporization of micro-droplet (SVM) method was investigated to lower the process cost and secure scalability.^[156] The rGO-coated metal foam compared with bare metal foam exhibited better performance owing to the enhanced mass transport and reduced interfacial contact resistance. The durability of the flow field also improved because of the coated rGO layers (Figure 11d). Through the SVM method, self-assembled 3D graphene (STG), which contains microscale-to-millyscale pores, was successfully constructed on the flat surface of a bipolar plate without using any backbone structure (Figure 11e). These intriguing 3D structures were formed using the SVM to spray rGO on the surface heated at 250 °C. During rapid vaporization, suspended rGO sheets were concentrated at the receding triple line, acting as a seed for the structures and developing into a porous network while the spray process was repeated. The 3D porous rGO structure exhibited high performance and sufficient feasibility for use as a flow field. Lee et al. further found that the conductivity of the STG flow field could be improved by thermal annealing up to 400 °C because it could reduce the Ohmic and kinetic resistances of fuel cells.^[157]

Even with these advantages of 3D porous fields, insufficient water removal capacity caused by the highly tortuous flow path still hinders their practical use (Figure 11f).^[162] To overcome this limitation, Jang et al. proposed a 3D graphene-coated Ni foam with patterned wettability through the selective functionalization of hydrophilic polymer materials to enhance water management.^[158] Multilayered graphene (MLG) was coated onto the pre-defined Ni foam through CVD, and oxygen plasma treatment was conducted using a metal mask with regular arrays of holes with a diameter of 300 μm and pitch size of 1.2 mm to selectively graft hydrophilic NVF. Based on the polarization curve, the single cell with MLG-coated Ni foam with patterned wettability was found to exhibit superior performance compared with the bare Ni foam, graphite channels with 1-mm serpentine channels, and MLG-coated Ni foam. The maximum performance of the MLG-coated Ni foam with a patterned hydrophilic region (920 mW cm⁻²) was 16% higher than that of


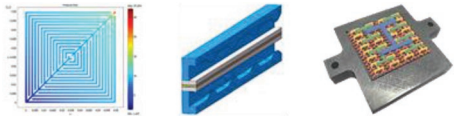

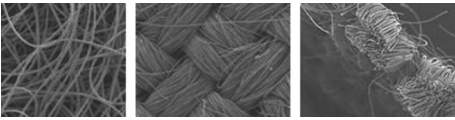
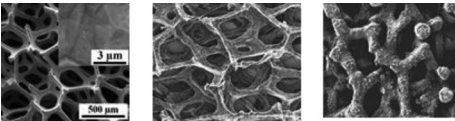
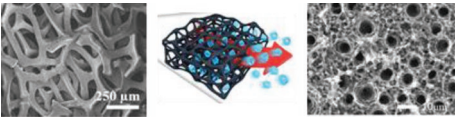
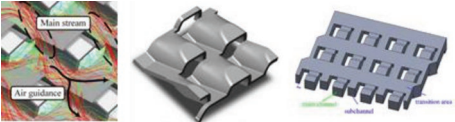
the conventional graphite channel (793 mW cm⁻²). In the EIS measurement results at high current density (1.6 A cm⁻²), the Ohmic resistance of the MLG-coated Ni foam compared with that of the bare Ni foam decreased. Moreover, the mass transport resistance decreased owing to the selective hydrophilic patterning. This enabled the preferential draining of water through the hydrophilic region, whereas the hydrophobic region acted as a gas transport pathway.

As another approach to 3D-structured flow fields, a 3D fine mesh was designed and applied to the flow field. The structure features an array of hundreds of micrometer-sized single baffles inclined at 26°. These inclined baffles function as air guides that induce forced convection (vertical to the bipolar plate) and contribute to the reactant supply and water removal from the GDL. Note that this 3D fine mesh has been used as a flow field in TOYOTA fuel cell vehicles because of its superiority in mass transport.^[163–167] Bao et al. investigated the two-phase flow characteristics in a 3D fine mesh. The morphology of the flow field of the 3D fine mesh was reconstructed based on observations. The flow characteristics were studied using the volume of fluid method, which was appropriate for the two-phase flow analysis (Figure 11g).^[37] Owing to the geometrical features of the baffle, the airflow was continuously guided toward the surface of the GDL with the convective flow vertical to the bipolar plate. Provided that the air velocity was not extremely low, the liquid droplet adhering to the surface of the baffles was pushed and moved to the area above the baffle owing to the air drag force, leading to less water cover on the GDL surface. This separate transport of liquid and gas facilitated the overall mass transport while effectively expelling water droplets. Although a stagnant area that the main streams could not reach existed, it only occupied less than 5% of the lower region volume, which barely limited the mass transport. As noted, considerable advances have been achieved based on the architecture strategy. The overall configurations and features of multiscale modifications for flow channels are summarized in **Table 4**.

4.3. Summary of Architected Transport Layer Approach

In this review, the previous research on architected GDLs with PG through MPL and carbon paper layer, micro-hole perforation via laser irradiation, and patterned wettability by selective functionalization have been introduced. These strategies have been proven to enable the effective removal of water from the transport layer and facilitate mass transport. These are achieved by reducing the breakthrough pressure from the catalyst side to the flow field side or separating the water and reactant gas pathways. Although it is evident the structural strategy is effective in alleviating water flooding, which leads to improved mass transport, the performance increment in low RH conditions or low current operating conditions is not noticeable as in the condition of water flooding. Rather, the improperly designed structure can accelerate drying in the electrode as the scarce water can be easily discharged throughout the GDL. Considering fuel cells operate in diverse conditions, including low RH conditions and low current density, the structural strategy should be effective for the diverse operating conditions. Hence,

Table 4. Summary of configurations and features of multiscale flow field modification.

Type	Material	Configurations	Feature	Main Improvements	Ref.
	Graphite/metal		Major flow channel geometries (parallel, serpentine, and interdigitated) of conventional bipolar plates	—	[2,168]
		Reproduced with permission. ^[168] Copyright 2021, Wiley-VCH.			
Pattern carved flow field	Graphite/metal		Novel bio-inspired optimal design for uniform reactant gas distribution for improving mass transport and minimizing pressure drop	Peak power density: 2.2–30% Pressure drop reduction: 50–70% (–51.2% for wave-like structure) Condition: RH 50–100, 70–75 °C	[36,154,155,168]
		Reproduced with permission. ^[154] Copyright 2009, Elsevier. Reproduced with permission. ^[155] Copyright 2020, Elsevier. Reproduced with permission. ^[36] Copyright 2018, Royal Society of Chemistry.			
	Metal foam (Al, Ni, NiCr, and Cu)		Dead zone minimized, high porosity, high mechanical strength, inadequate corrosion resistance, and low cost	Peak power density: 38.1–78% Total current density: 56.8–82% Condition: RH 50–100, 60–70 °C	[158,169,170,189]
		Reproduced with permission. ^[189] Copyright 2019, Elsevier. Reproduced with permission. ^[169] Copyright 2012, Elsevier. Reproduced with permission. ^[170] Copyright 2018, Elsevier.			
	Carbon felt/cloth		Dead zone minimized, relatively low porosity, relatively low mechanical strength, high corrosion resistance, and relatively low cost	Total current density: 16.4% Kinetic loss reduction: 55.50% Condition: RH 100, 75 °C	[171,172]
		Reproduced with permission. ^[171] Copyright 2012, Elsevier. Reproduced with permission. ^[172] Copyright 2019, ECS.			
3D porous media flow field	Graphene-coated metal foam		Dead zone minimized, high porosity, high mechanical strength, high corrosion resistance, and relatively high cost	Peak power density: 32.7–51.7% Kinetic loss reduction: 48.2–58.5% ICR ^{a)} reduction: 35.5–68.7% Condition: RH 50–100, 60–70 °C	[156,158,173]
		Reproduced with permission. ^[156] Copyright 2020, Elsevier. Adapted with permission from. ^[158] Copyright 2019, American Chemical Society. Reproduced with permission. ^[173] Copyright 2018, Royal Society of Chemistry.			
	3D graphene foam/ Self-assembled 3D rGO		Dead zone minimized, high porosity, relatively low mechanical strength, high corrosion resistance, and relatively high cost	Peak power density: 14.9–28.6% Total current density: 20.8–32.5% Kinetic loss reduction: 17.5–70.6% Condition: RH 100, 60–65 °C	[156,160,173]
		Reproduced with permission. ^[156] Copyright 2020, Elsevier. Reproduced with permission. ^[160] Copyright 2018, Elsevier.			
	3D fine mesh		Improved forced convection of reactant gas and produced water, high mechanical strength	Peak power density: 15.4% Total current density: 33.7–48.8% Condition: RH 100, 60–80 °C	[37,163,167,174]
		Reproduced with permission. ^[37] Copyright 2019, Elsevier. Reproduced with permission. ^[174] Copyright 2020, Elsevier.			

^{a)}ICR: Interfacial contact resistance.

it is still required to develop structurally modified GDL, which is effective even in low humidity and dry state while facilitating water removal in water flooding states. As one of the future development directions, next-generation GDLs can be responsive to changes in the operating conditions by self-modifying pore structures and wettability depending on the diverse conditions.^[175–177] And, most research utilized dual-layers to generate PG, single-scale perforation in perforated GDL, and discrete hydrophobic and hydrophilic regions without gradient. In this aspect, more complex multilayers and multiscale approaches can be explored to maximize their effects on improving mass transport. Furthermore, in the aspect of commercial use of GDLs, large area fabrication and mass production should be considered. For instance, the micro-sized perforation was conducted with the laser technique, which is limited to applying in a large area and mass production. The plasma etching process with an etching mask and electrical discharge machining with an arrayed electrode can be applied to fabricate the perforated GDLs.^[178–181] Last, based on the fact the thickness of GDLs should be slightly higher than the thickness of the gasket to obtain lower interfacial resistance, and good electrical contact between bipolar plate and electrode, the structural stability and compressibility of GDLs should be scrutinized. Since the structurally modified GDLs inevitably have more void space than the conventional ones, mechanical deformation during the compression may induce the structural collapse of the pores. Hence, the design rule for permissible porosity and compressibility depending on the modified structures should be explored to be used as commercial GDLs.

When it comes to flow channel modification, research on the bio-inspired flow field, 3D porous media flow field, and 3D fine mesh has been reviewed. Bio-inspired flow channels are effective to minimize pressure drop and obtain uniform reactant gas distribution. And 3D porous media flow fields minimize the dead zone between GDL and channel, and the microstructured rib of the foam leads to improved reactant utilization. And 3D fine mesh with tilted baffle structures highly improves mass transport by inclined convective force. Although most developed flow channels are proven to be effective for enhancing mass transport, the effects in diverse conditions reflecting real operating conditions for each application (e.g., vehicle power pack and power plant) have not been fully investigated. In addition, the effect of reduced pressure drop in the bio-inspired channel in a simulation study should be considered with the liquid water continuously supplied to the channel from the GDL, and further experimental validation should be followed. And based on the fact that the bipolar plate, on which the flow channel is directly carved or assembled, is an electron collector and transfer pathway, the material used in the bipolar plate and flow channel should be highly conductive and chemical resistant. Depending on the used material, channel size and configuration are restricted to be manufactured due to the processability of the materials. As the channel configuration becomes more complex and the channel size gets narrower, the processability of the channel becomes more crucial. Emerging technology such as 3D metal printing can be applied to realize the complex and novel flow channel with a low cost.^[182–184] And from a practical point of view, among the fuel cell components, the bipolar plate takes the most portion in weight, volume, and

cost.^[185,186] As the fuel cell application requires lightweight and reduced volume, the weight and volume of the bipolar channel should be considered as well as the flow channel design. Finally, further investigation on combining the effect of the channel morphology and surface wettability will be needed to resolve the mass transport issue.

5. Conclusion and Perspective

In conclusion, diverse multiscale architecting technologies for modifying and reconstructing the structure of membranes, electrodes, and transport layers for realizing high-performance and reliable PEMFCs are comprehensively presented in this review. The key advances in each composition are summarized as follows.

- 1) Multiscale patterned membranes: A patterned membrane can provide an enlarged membrane–electrode interfacial contact area and affect the morphology of each membrane and electrode. The expanded interfacial area between the membrane and the electrode can lead to an increase of L_C in Equation (2) which brings high ECSA values while using the same amount of catalyst. And, the locally thinned membrane and the extruded part of the Nafion membrane inside the electrode can affect the reduction of Ohmic overpotential in Equation (3). Furthermore, the modified electrode morphology can effectively reduce the mass transport resistance in Equation (5) by changing ε in the electrode and forming macro-voids at the interface between the electrode and the GDL. With the use of patterned membranes, the modified MEAs exhibited much higher peak power densities up to $\approx 70\%$ compared to the MEAs with flat membranes. Based on their morphological characteristics, diverse membrane surface-patterning strategies are categorized into random, single-scale, and multiscale structures. In the case of random structuring, plasma-induced ion bombardment, sacrificial templating with metal–oxide nanowire/rod, solvent evaporation method with a high-boiling-point solvent, and an electric field-assisted rugged surface structure were introduced. To construct a well-designed single-scale structure, a direct e-beam patterning method has been devised. However, most recent studies have adopted the thermal imprinting process with the advantage of reproducibility and process efficiency. Structural optimization for maximizing the catalyst utilization with diverse pattern shapes and sizes, as well as improved water removal from asymmetrically designed membrane/electrode structures based on Laplace pressure difference were presented. Finally, novel strategies for introducing multiscale structures on the membrane surface with the use of successive imprinting processes and multiscale multilevel structured mold were examined. With the structural advantage of simultaneously employing microscale and nanoscale morphologies, the multiscale architecting strategies confirmed their efficacy by exhibiting outperforming PEMFC performance than that of single-scale structures used for constructing multiscale structures. However, there are still limitations to adopting the surface patterning methodology for industrial application, because all the studies verified

the effects with the MEA of a small active area and applying direct spray deposition to conformally construct the electrode on the patterned membrane. And, the quantitative effects for increasing ECSA and reducing Ohmic and charge transport resistance are quite different for each study even under similar pattern shape and surface area increment. Therefore, it is necessary to accurately verify the patterned membrane effects in the large-area MEA with the development of an industrial applicable large-area direct catalyst-coating method as well as membrane patterning technique. In addition, it is desirable to adopt well-accepted standardized protocols (e.g., DOE protocol) for unifying the MEA evaluation environment as well as reference membrane, electrode configuration, and porous transport layer for accurate comparison between the structures and finding out the optimal pattern design.

- 2) Multiscale architected electrode: The development of strategies for modifying the electrode structure to improve the utilization of the catalyst and mass transfer (lowering η_{kinetic} and η_{mass}) is critical for the realization of high-performance PEMFCs. The structure of electrodes was tailored to secure macropores by adding pore formers and generating controlled cracks, which enabled high oxygen transport and water removal capacity. Moreover, different from the conventional 2D flat structure of electrodes, the architected electrodes were constructed to have 1D (e.g., VACNT electrode), 3D (e.g., IO structure electrode), and multiscale multilevel (e.g., 3D grid-patterned electrode) structures that exhibited a high oxygen transport capacity even with low catalyst loading, resulting in performance improvement by up to two-fold compared to reference MEAs, as well as high electrode durability due to their carbon-free nature. However, for the application of electrode structure modification strategies in a real PEMFC system, many technical issues must be tackled. First, the introduction of pore-formers and intentional cracks may have durability issues because the processes can damage each component of the MEA during electrode modification, and lower the mechanical strength of the completed electrode. In the case of the multiscale structured 1D and 3D electrode structures, they have many technical issues such as manufacturing complexity, relatively low productivity, and difficulty in the preparation of large-area electrode. No matter how advantageous the characteristics of structurally modified electrodes are for the MEA performance, it will be more meaningful when the unconventional electrodes exhibit the high feasibility and applicability for actual PEMFCs system rather than just a lab-scale experiment, as shown by Toyota's work for the 1D Pt/VACNT electrodes.
- 3) Multiscale functional transport layer: As for the GDLs as a transport layer, the PG in the GDL are stacked from fine to coarse structures in the form of fiber and particle aggregates. It enables effective water management by gradually reducing the breakthrough pressure throughout the transport layer, which leads to enhanced power density by up to 131% compared to the commercial one. The perforated GDL (mainly processed by laser beam irradiation) and the GDL with patterned wettability (obtained through selective functionalization with hydrophilic materials, such as AA and NVF) are effective for water management. They provide a favorable pathway for water through the perforated and hydrophilic regions, respectively. The spatially

controlled porosity and wettability through GDLs effectively discharge the liquid water, which blocks the pores and reduces porosity inside the electrode and GDLs, to the outside, which leads to the increased effective diffusivity (D_{eff}) in Equation (5) of the reactant and decreased concentration overpotential. And multiscale engineered flow channels inspired by the leaf and lung designs were investigated to effectively distribute the reactant gas to the electrode while minimizing the pressure drop by up to 70% through the channel. As another type of channel, 3D porous flow fields with high chemical resistance and that are capable of minimizing the dead zone where the ribs of the channel and GDL surface are in contact have been extensively studied. Well-designed pore distribution and size with proper compression ratio improve power density by up to 78% compared to the conventional channel. Further, a 3D fine mesh was designed with hundreds of micrometer-sized baffles. The mesh, which induced the convective flow vertical to the bipolar plate, was introduced and successfully implemented in commercial fuel cell vehicles because of its superiority in mass transport. In the previous studies, although many advances in the transport layer have been achieved, the structural strategy can be further advanced by investigating the effects in diverse operating conditions, including flow rate, RH, operating temperature, and back pressure. And in-depth approaches with more complex multilayers and multiscale structures while considering mass production processability can be explored to maximize their effects on enhancing mass transport. Furthermore, the mechanical deformation of the modified GDLs during the compression in the assembly process, which may induce the structural collapse of the designed pores, should be further studied. In addition, the combining effect of surface wettability with the channel design to improve mass transport can be investigated. And in-depth simulation study considering multi-phase flow, which accurately reflects liquid water supply from GDL and behavior in the channel, and following experimental validation will be required. Considering the material choice and complexity of the channel, emerging technology such as 3D metal printing can be applied to manufacture diverse flow channels at a low cost. Finally, since the bipolar plate takes the most portion in weight, volume, and cost among the fuel cell components, a novel design considering weight, volume, and cost will be needed for commercial implementation.

Overall, many remarkable advancements have been achieved in PEMFC components through architecturing strategies. However, most studies solely focused on the effect of each part without considering the synergistic effects of combining the developed components into a single-cell assembly. In this regard, considerable effort is required to combine and integrate each of the high-performing components to achieve a big leap to next-level development. For example, pore structure, porosity, and pore-size distribution were treated as critical parameters affecting the mass transport in the MEA by modifying each part. That is, the pore structures can be designed to be graded and have low threshold pressure through the membrane, electrode, MPL, carbon paper, and flow channel in serial while securing the mechanical stability and connection between them. And this strategy for improving mass transport can be expanded

to the stack system from the single cell level. When it comes to the commercialization potential of the introduced technologies for industrial application, some key technologies (e.g., 3D fine mesh) have been successfully commercialized in the fuel cell market based on successful mass production processes; however, most of other technologies remain in the laboratory-scale development stage. This is because of the size limitation of the applied multiscale structures, discontinuous production processes, and small-scale production in laboratory-scale chemical reactors. Also, when considering the MEA manufacturing method, most studies adopted a spray deposition with an airbrush, suitable for small-area scales, to conformally construct the electrode on the patterned membrane. The decal transfer method, currently most used in industry, is not compatible with the patterned membrane, because it is performed above the glass transition temperature of Nafion. In that condition, the structure on the membrane can be disappeared as the patterned membrane may get flattened, and the void spaces may not be filled with catalysts. Therefore, it is required to develop other direct-coating methods that can be applied to large-area and roll-to-roll processes having high technology maturity in the industry, such as slot-die coating and ink-jet printing.^[187,188] And, a strong bond between the academe and industry must be established. This can be achieved through continuous discussions and collaborations, implementation of mass production processes of potential candidate component technology at the pilot and industrial scales, and validation of notable effects at the commercial level. As a last remark, for fair comparison and accurate evaluation of the developed technologies, single-cell tests should be conducted under well-defined and standardized operating conditions and protocols with comparable MEA compositions. Since most of the fuel tests in the research papers have not been comparable due to the difference in MEA composition, operating condition, and protocol, the improved results can be overinterpreted and valid only in the specific condition. And there have been few studies reporting the reproducibility and repeatability of the architectures and the structural effects. The studies on the architecturing strategy should further provide reproducibility of the structures as well as the repeatability of the impact of the structures on device performance. And the fabrication process and steps should be provided in detail to be reproducibly constructed by readers and other researchers. In these aspects, standard protocols for evaluating performance, reproducibility, and repeatability should be established through active collaboration between the academe and the industry field. And it needs for researchers to be encouraged to address these issues based on the standard protocols.

Acknowledgements

S.J. and Y.S.K. contributed equally to this work. This study was supported by the National Research Foundation (NRF) of Korea (Grant Nos. 2021M3H4A1A02042948 and 2021M3H4A1A02042957).

Conflict of Interest

The authors declare no conflict of interest.

Keywords

electrodes, membranes, multiscale architecturing, polymer electrolyte membrane fuel cells, transport layers

Received: May 31, 2022

Revised: August 28, 2022

Published online: March 11, 2023

- [1] H. A. Gasteiger, N. M. Marković, *Science* **2009**, 324, 48.
- [2] R. O'hayre, S.-W. Cha, W. Colella, F. B. Prinz, *Fuel Cell Fundamentals*, John Wiley & Sons, New York **2016**.
- [3] C. K. Dyer, *J. Power Sources* **2002**, 106, 31.
- [4] T. Li, L. Huang, H. Liu, *Energy* **2019**, 172, 840.
- [5] L. D. Paulson, *Computer* **2003**, 36, 10.
- [6] K. Kim, T. Kim, K. Lee, S. Kwon, *J. Power Sources* **2011**, 196, 9069.
- [7] V. P. McConnell, *Fuel Cells Bull.* **2007**, 2007, 12.
- [8] T. Keränen, H. Karimäki, J. Viitakangas, J. Vallet, J. Ihonen, P. Hyöttylä, H. Uusalo, T. Tingelöf, *J. Power Sources* **2011**, 196, 9058.
- [9] A. Serov, C. Kwak, *Appl. Catal., B* **2009**, 90, 313.
- [10] J. K. Nørskov, J. Rossmeisl, A. Logadottir, L. Lindqvist, J. R. Kitchin, T. Bligaard, H. Jonsson, *J. Phys. Chem. B* **2004**, 108, 17886.
- [11] Y.-J. Wang, W. Long, L. Wang, R. Yuan, A. Ignaszak, B. Fang, D. P. Wilkinson, *Energy Environ. Sci.* **2018**, 11, 258.
- [12] T. Mennola, M. Mikkola, M. Noponen, T. Hottinen, P. Lund, *J. Power Sources* **2002**, 112, 261.
- [13] S. Lee, S. Mukerjee, J. McBreen, Y. Rho, Y. Kho, T. Lee, *Electrochim. Acta* **1998**, 43, 3693.
- [14] T. A. Suter, K. Smith, J. Hack, L. Rasha, Z. Rana, G. M. A. Angel, P. R. Shearing, T. S. Miller, D. J. Brett, *Adv. Energy Mater.* **2021**, 11, 2101025.
- [15] M. Breitwieser, M. Klingele, S. Vierrath, R. Zengerle, S. Thiele, *Adv. Energy Mater.* **2018**, 8, 1701257.
- [16] Y. Ke, W. Yuan, F. Zhou, W. Guo, J. Li, Z. Zhuang, X. Su, B. Lu, Y. Zhao, Y. Tang, *Renewable Sustainable Energy Rev.* **2021**, 145, 110860.
- [17] A. Kusoglu, A. Z. Weber, *Chem. Rev.* **2017**, 117, 987.
- [18] S. Ahmad, T. Nawaz, A. Ali, M. F. Orhan, A. Samreen, A. M. Kannan, *Int. J. Hydrogen Energy* **2022**, 47, 19086.
- [19] K. R. Yoon, K. A. Lee, S. Jo, S. H. Yook, K. Y. Lee, I.-D. Kim, J. Y. Kim, *Adv. Funct. Mater.* **2019**, 29, 1806929.
- [20] K. H. Oh, H. S. Kang, M. J. Choo, D. H. Jang, D. Lee, D. G. Lee, T. H. Kim, Y. T. Hong, J. K. Park, H. T. Kim, *Adv. Mater.* **2015**, 27, 2974.
- [21] C. H. Park, S. Y. Lee, D. S. Hwang, D. W. Shin, D. H. Cho, K. H. Lee, T. W. Kim, T. W. Kim, M. Lee, D. S. Kim, C. M. Doherty, A. W. Thornton, A. J. Hill, M. D. Guiver, Y. M. Lee, *Nature* **2016**, 532, 480.
- [22] H. Zhu, *Joule* **2022**, 6, 718.
- [23] R. S.-L. Yee, R. A. Rozendal, K. Zhang, B. P. Ladewig, *Chem. Eng. Res. Des.* **2012**, 90, 950.
- [24] C.-Y. Ahn, S. Jang, Y.-H. Cho, J. Choi, S. Kim, S. M. Kim, Y.-E. Sung, M. Choi, *Sci. Rep.* **2018**, 8, 6085.
- [25] S. Jang, M. Her, S. Kim, J.-H. Jang, J. E. Chae, J. Choi, M. Choi, S. M. Kim, H.-J. Kim, Y.-H. Cho, *ACS Appl. Mater. Interfaces* **2019**, 11, 34805.
- [26] S. J. Bae, S. J. Yoo, Y. Lim, S. Kim, Y. Lim, J. Choi, K. S. Nahm, S. J. Hwang, T.-H. Lim, S.-K. Kim, *J. Mater. Chem.* **2012**, 22, 8820.
- [27] J. Wang, Q. Xue, B. Li, D. Yang, H. Lv, Q. Xiao, P. Ming, X. Wei, C. Zhang, *ACS Appl. Mater. Interfaces* **2020**, 12, 7047.
- [28] W. Li, P. Halder, *Electrochem. Solid-State Lett.* **2010**, 13, B47.
- [29] J. M. Kim, A. Jo, K. A. Lee, H. J. Han, Y. J. Kim, H. Y. Kim, G. R. Lee, M. Kim, Y. Park, Y. S. Kang, *Sci. Adv.* **2021**, 7, eabe9083.
- [30] S. Murata, M. Imanishi, S. Hasegawa, R. Namba, *J. Power Sources* **2014**, 253, 104.

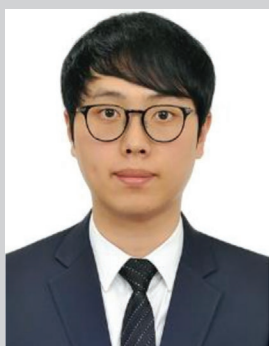
- [31] S. M. Kim, C. Y. Ahn, Y. H. Cho, S. Kim, W. Hwang, S. Jang, S. Shin, G. Lee, Y. E. Sung, M. Choi, *Sci. Rep.* **2016**, *6*, 26503.
- [32] Y. Yang, X. Zhou, B. Li, C. Zhang, *Int. J. Hydrogen Energy* **2021**, *46*, 4259.
- [33] S. Zhang, H. Xu, Z. Qu, S. Liu, F. K. Talkhonchek, *J. Power Sources* **2022**, *522*, 231003.
- [34] L. Zhao, J. Zhu, Y. Zheng, M. Xiao, R. Gao, Z. Zhang, G. Wen, H. Dou, Y. P. Deng, A. Yu, Z. Wang, Z. Chen, *Adv. Energy Mater.* **2021**, *12*, 2102665.
- [35] A. Aiyajina, M. Sastry, *J. Fuel Cell Sci. Technol.* **2012**, *9*.
- [36] P. Trogadas, J. Cho, T. Neville, J. Marquis, B. Wu, D. Brett, M.-O. Coppens, *Energy Environ. Sci.* **2018**, *11*, 136.
- [37] Z. Bao, Z. Niu, K. Jiao, *J. Power Sources* **2019**, *438*, 226995.
- [38] H. Cho, S. M. Kim, Y. S. Kang, J. Kim, S. Jang, M. Kim, H. Park, J. W. Bang, S. Seo, K. Y. Suh, Y. E. Sung, M. Choi, *Nat. Commun.* **2015**, *6*, 8484.
- [39] C. Spiegel, *Designing and Building Fuel Cells*, McGraw-Hill, New York, **2007**.
- [40] J. Lee, C. Seol, J. Kim, S. Jang, S. M. Kim, *Energy Technol.* **2021**, *9*, 2100113.
- [41] F. Barbir, *PEM Fuel Cells: Theory and Practice*, Academic Press, **2012**.
- [42] C. H. Lee, R. Banerjee, F. Arbabi, J. Hinebaugh, A. Bazylak, in *Int. Conf. on Nanochannels, Microchannels, and Minichannels*, American Society of Mechanical Engineers, New York **2016**, p. 50343/V001T07A003.
- [43] C. Lamy, D. J. Jones, C. Coutanceau, P. Brault, S. Martemianov, Y. Bultel, *Electrochim. Acta* **2011**, *56*, 10406.
- [44] Y. Jeon, D. J. Kim, J. K. Koh, Y. Ji, J. H. Kim, Y. G. Shul, *Sci. Rep.* **2015**, *5*, 16394.
- [45] J. K. Koh, Y. Jeon, Y. I. Cho, J. H. Kim, Y.-G. Shul, *J. Mater. Chem. A* **2014**, *2*, 8652.
- [46] I. Fouzaï, S. Gentil, V. C. Bassetto, W. O. Silva, R. Maher, H. H. Girault, *J. Mater. Chem. A* **2021**, *9*, 11096.
- [47] K. K. Karuppanan, A. V. Raghun, M. K. Panthalingal, S. Ramanathan, T. Kumaresan, B. Pullithadathil, *J. Mater. Chem. A* **2018**, *6*, 12768.
- [48] M. C. Lefebvre, R. B. Martin, P. G. Pickup, *Electrochem. Solid-State Lett.* **1999**, *2*, 259.
- [49] H. Matsuda, K. Fushinobu, A. Ohma, K. Okazaki, *J. Therm. Sci. Technol.* **2011**, *6*, 154.
- [50] L. Ye, Y. Gao, S. Zhu, J. Zheng, P. Li, J. P. Zheng, *Int. J. Hydrogen Energy* **2017**, *42*, 7241.
- [51] M. T. Y. Paul, M. S. Saha, W. L. Qi, J. Stumper, B. D. Gates, *Int. J. Hydrogen Energy* **2020**, *45*, 1304.
- [52] V. B. K. P. G. Varghese, T. V. Joseph, P. Chippar, *Int. J. Hydrogen Energy* **2022**, *47*, 33014.
- [53] A. Omosebi, R. S. Besser, *ECS Trans.* **2011**, *41*, 883.
- [54] M. Aizawa, H. Gyoten, *J. Electrochem. Soc.* **2013**, *160*, F417.
- [55] L. Pu, J. Jiang, T. Yuan, J. Chai, H. Zhang, Z. Zou, X.-M. Li, H. Yang, *Appl. Surf. Sci.* **2015**, *327*, 205.
- [56] M. Chen, M. Wang, Z. Yang, X. Ding, Q. Li, X. Wang, *Electrochim. Acta* **2018**, *263*, 201.
- [57] S. M. Kim, Y. S. Kang, C. Ahn, S. Jang, M. Kim, Y.-E. Sung, S. J. Yoo, M. Choi, *J. Power Sources* **2016**, *317*, 19.
- [58] J. Choi, J. H. Yeon, S. H. Yook, S. Shin, J. Y. Kim, M. Choi, S. Jang, *ACS Appl. Mater. Interfaces* **2021**, *13*, 806.
- [59] S. Kang, G. Bae, S.-K. Kim, D.-H. Jung, Y.-G. Shul, D.-H. Peck, *Int. J. Hydrogen Energy* **2018**, *43*, 11386.
- [60] Y. V. Yakovlev, J. Nováková, P. Kúš, T. N. Dinová, I. Matolínová, V. Matolín, *J. Power Sources* **2019**, *439*, 227084.
- [61] J.-W. Ha, S. Park, *Macromol. Res.* **2016**, *25*, 1.
- [62] T. Hrbek, P. Kúš, Y. Yakovlev, J. Nováková, Y. Lobko, I. Khalakhan, V. Matolín, I. Matolínová, *Int. J. Hydrogen Energy* **2020**, *45*, 20776.
- [63] J. H. Kim, J. Sohn, J. H. Cho, M. Y. Choi, I. G. Koo, W. M. Lee, *Plasma Processes Polym.* **2008**, *5*, 377.
- [64] A. Omosebi, R. Besser, *Fuel Cells* **2017**, *17*, 762.
- [65] Z. Ogumi, Y. Uchimoto, M. Tsujikawa, Z. Takehara, F. Foulkes, *J. Electrochem. Soc.* **1990**, *137*, 1430.
- [66] R. O'hayre, S.-J. Lee, S.-W. Cha, F. B. Prinz, *J. Power Sources* **2002**, *109*, 483.
- [67] M. Prasanna, E. Cho, H.-J. Kim, T.-H. Lim, I.-H. Oh, S.-A. Hong, *J. Power Sources* **2006**, *160*, 90.
- [68] S. Cho, E. Cho, I.-H. Oh, H.-J. Kim, H. Ha, S.-A. Hong, J. Ju, *J. Power Sources* **2006**, *155*, 286.
- [69] Y.-H. Cho, J. W. Bae, Y.-H. Cho, J. W. Lim, M. Ahn, W.-S. Yoon, N.-H. Kwon, J. Y. Jho, Y.-E. Sung, *Int. J. Hydrogen Energy* **2010**, *35*, 10452.
- [70] W. S. Chi, Y. Jeon, S. J. Park, J. H. Kim, Y.-G. Shul, *ChemPlusChem* **2014**, *79*, 1109.
- [71] Q. K. Dang, D. Henkensmeier, N. N. Krishnan, J. H. Jang, H.-J. Kim, S. W. Nam, T.-H. Lim, *J. Membr. Sci.* **2014**, *460*, 199.
- [72] F. Ning, C. Bai, J. Qin, Y. Song, T. Zhang, J. Chen, J. Wei, G. Lu, H. Wang, Y. Li, J. Gu, Y. Shen, Y. Cui, Y. Huang, X. Zhou, *J. Mater. Chem. A* **2020**, *8*, 5489.
- [73] S. K. Babu, R. W. Atkinson, A. B. Papandrew, S. Litster, *ChemElectroChem* **2015**, *2*, 1752.
- [74] D. Joseph, J. Büssemann, C. Harms, D. Henkensmeier, M. J. Larsen, A. Dyck, J. H. Jang, H.-J. Kim, S. W. Nam, *J. Membr. Sci.* **2016**, *520*, 723.
- [75] S. Choi, S. Yuk, D.-H. Lee, G. Doo, D. W. Lee, M.-J. Choo, H.-T. Kim, *Electrochim. Acta* **2018**, *268*, 469.
- [76] J. B. Ballengee, P. N. Pintauro, *Macromolecules* **2011**, *44*, 7307.
- [77] J. W. Park, R. Wycisk, P. N. Pintauro, *J. Membr. Sci.* **2015**, *490*, 103.
- [78] S. Martin, B. Martinez-Vazquez, P. Garcia-Ybarra, J. Castillo, *J. Power Sources* **2013**, *229*, 179.
- [79] S. Martin, P. Garcia-Ybarra, J. Castillo, *Int. J. Hydrogen Energy* **2010**, *35*, 10446.
- [80] L. Zhang, T. Porter, S. Guillory, C. Chi, C. G. Arges, *ECS Trans.* **2017**, *77*, 1325.
- [81] Y. Zhang, J. Lu, S. Shimano, H. Zhou, R. Maeda, *Electrochem. Commun.* **2007**, *9*, 1365.
- [82] C. Seol, S. Jang, J. Lee, L. V. Nam, T. A. Pham, S. Koo, K. Kim, J.-H. Jang, S. M. Kim, S. J. Yoo, *ACS Sustainable Chem. Eng.* **2021**, *9*, 5884.
- [83] A. Omosebi, R. S. Besser, *J. Electrochem. Soc.* **2011**, *158*, D603.
- [84] A. Omosebi, R. S. Besser, *J. Power Sources* **2013**, *228*, 151.
- [85] Y.-H. Cho, J. W. Bae, O.-H. Kim, J. Y. Jho, N. Jung, K. Shin, H. Choi, H. Choe, Y.-H. Cho, Y.-E. Sung, *J. Membr. Sci.* **2014**, *467*, 36.
- [86] M. Wang, G. Liu, Z. Tian, Y. Shao, L. Wang, F. Ye, M. X. Tran, Y. Yun, J. K. Lee, *Energy Convers. Manage.* **2017**, *148*, 753.
- [87] J. W. Bae, Y.-H. Cho, Y.-E. Sung, K. Shin, J. Y. Jho, *J. Ind. Eng. Chem.* **2012**, *18*, 876.
- [88] Q. Wang, M. Eikerling, D. Song, Z. Liu, T. Navessin, Z. Xie, S. Holdcroft, *J. Electrochem. Soc.* **2004**, *151*, A950.
- [89] S. Jang, M. Kim, Y. S. Kang, Y. W. Choi, S. M. Kim, Y. E. Sung, M. Choi, *ACS Appl. Mater. Interfaces* **2016**, *8*, 11459.
- [90] W. G. Bae, H. N. Kim, D. Kim, S. H. Park, H. E. Jeong, K. Y. Suh, *Adv. Mater.* **2014**, *26*, 675.
- [91] H. Cho, J. Kim, H. Park, J. W. Bang, M. S. Hyun, Y. Bae, L. Ha, D. Y. Kim, S. M. Kang, T. J. Park, S. Seo, M. Choi, K. Y. Suh, *Nat. Commun.* **2014**, *5*, 3137.
- [92] D. H. Lee, G. T. Yun, G. Doo, S. Yuk, H. Guim, Y. Kim, W. B. Jung, H. T. Jung, H. T. Kim, *Nano Lett.* **2022**, *22*, 1174.
- [93] R. Makharia, M. F. Mathias, D. R. Baker, *J. Electrochem. Soc.* **2005**, *152*, A970.
- [94] T. Schuler, A. Chowdhury, A. T. Freiberg, B. Sneed, F. B. Spingler, M. C. Tucker, K. L. More, C. J. Radke, A. Z. Weber, *J. Electrochem. Soc.* **2019**, *166*, F3020.
- [95] R. N. Carter, S. S. Kocha, F. Wagner, M. Fay, H. A. Gasteiger, *ECS Trans.* **2007**, *11*, 403.

- [96] M. Aizawa, H. Gyoten, A. Salah, X. Liu, *J. Electrochem. Soc.* **2010**, *157*, B1844.
- [97] M. K. Debe, *Nature* **2012**, *486*, 43.
- [98] Z. Ma, Z. P. Cano, A. Yu, Z. Chen, G. Jiang, X. Fu, L. Yang, T. Wu, Z. Bai, J. Lu, *Angew. Chem., Int. Ed. Engl.* **2020**, *59*, 18334.
- [99] N. Jung, D. Y. Chung, J. Ryu, S. J. Yoo, Y.-E. Sung, *Nano Today* **2014**, *9*, 433.
- [100] C. Y. Ahn, J. E. Park, S. Kim, O. H. Kim, W. Hwang, M. Her, S. Y. Kang, S. Park, O. J. Kwon, H. S. Park, Y. H. Cho, Y. E. Sung, *Chem. Rev.* **2021**, *121*, 15075.
- [101] T. A. M. Suter, A. J. Clancy, N. R. Carrero, M. Heitzmann, L. Guetaz, P. R. Shearing, C. Mattevi, G. Gebel, C. A. Howard, M. S. P. Shaffer, P. F. McMillan, D. J. L. Brett, *Nanomaterials* **2021**, *11*, 2530.
- [102] S. Kattamanchi, K. Palakurthi, P. Haridoss, *Energy Technol.* **2020**, *8*, 2000119.
- [103] Y.-H. Cho, N. Jung, Y. S. Kang, D. Y. Chung, J. W. Lim, H. Choe, Y.-H. Cho, Y.-E. Sung, *Int. J. Hydrogen Energy* **2012**, *37*, 11969.
- [104] S. Waseem, P. H. Maheshwari, P. Maheshwari, A. K. Sahu, A. Saini, S. R. Dhakate, *Energy Fuels* **2020**, *34*, 16736.
- [105] M. Uchida, Y.-C. Park, K. Kakinuma, H. Yano, D. A. Tryk, T. Kamino, H. Uchida, M. Watanabe, *Phys. Chem. Chem. Phys.* **2013**, *15*, 11236.
- [106] D. Li, Y. Qu, J. Liu, W. He, H. Wang, Y. Feng, *J. Power Sources* **2014**, *272*, 909.
- [107] C. S. Kong, D.-Y. Kim, H.-K. Lee, Y.-G. Shul, T.-H. Lee, *J. Power Sources* **2002**, *108*, 185.
- [108] S. Kjelstrup, M.-O. Coppens, J. Pharoah, P. Pfeifer, *Energy Fuels* **2010**, *24*, 5097.
- [109] M. Cannio, S. Righi, P. E. Santangelo, M. Romagnoli, R. Pedicini, A. Carbone, I. Gatto, *Renewable Energy* **2021**, *163*, 414.
- [110] A. Fischer, J. Jindra, H. Wendt, *J. Appl. Electrochem.* **1998**, *28*, 277.
- [111] K. C. Kil, S.-G. Hong, J. O. Park, C. Pak, H. Chang, U. Paik, *Int. J. Hydrogen Energy* **2014**, *39*, 17481.
- [112] A. Zlotorowicz, K. Jayasayee, P. I. Dahl, M. S. Thomassen, S. Kjelstrup, *J. Power Sources* **2015**, *287*, 472.
- [113] X. Cheng, C. Wang, G. Wei, X. Yan, S. Shen, C. Ke, F. Zhu, J. Zhang, *J. Electrochem. Soc.* **2019**, *166*, F1055.
- [114] M. Alias, S. Kamarudin, A. Zainoodin, M. Masdar, *Int. J. Energy Res.* **2021**, *45*, 12928.
- [115] J. Li, H. Tang, R. Chen, D. Liu, Z. Xie, M. Pan, S. P. Jjiang, *J. Mater. Chem. A* **2015**, *3*, 15001.
- [116] Y. Zeng, H. Zhang, Z. Wang, J. Jia, S. Miao, W. Song, Y. Xiao, H. Yu, Z. Shao, B. Yi, *J. Mater. Chem. A* **2018**, *6*, 6521.
- [117] R. Deng, Z. Xia, R. Sun, S. Wang, G. Sun, *J. Energy Chem.* **2020**, *43*, 33.
- [118] R. Wang, D. C. Higgins, D. U. Lee, S. Prabhudev, F. M. Hassan, V. Chabot, G. Lui, G. Jiang, J.-Y. Choi, L. Rasenthiram, J. Fu, G. Botton, Z. Chen, *Nano Energy* **2016**, *20*, 57.
- [119] Y. Zeng, Z. Shao, H. Zhang, Z. Wang, S. Hong, H. Yu, B. Yi, *Nano Energy* **2017**, *34*, 344.
- [120] R. Sun, Z. Xia, L. Shang, X. Fu, H. Li, S. Wang, G. Sun, *J. Mater. Chem. A* **2017**, *5*, 15260.
- [121] M. Qi, Y. Zeng, M. Hou, Y. Gou, W. Song, H. Chen, G. Wu, Z. Jia, Y. Gao, H. Zhang, Z. Shao, *Appl. Catal., B* **2021**, *298*, 120504.
- [122] J. Lee, J. M. Yoo, Y. Ye, Y. Mun, S. Lee, O. H. Kim, H. W. Rhee, H. I. Lee, Y. E. Sung, J. Lee, *Adv. Energy Mater.* **2015**, *5*, 1402093.
- [123] E. Antolini, *Appl. Catal., B* **2009**, *88*, 1.
- [124] J. C. Meier, C. Galeano, I. Katsounaros, J. Witte, H. J. Bongard, A. A. Topalov, C. Baldizzone, S. Mezzavilla, F. Schüth, K. J. Mayrhofer, *Beilstein J. Nanotechnol.* **2014**, *5*, 44.
- [125] Y. Shao, J. Liu, Y. Wang, Y. Lin, *J. Mater. Chem.* **2009**, *19*, 46.
- [126] O. H. Kim, Y. H. Cho, S. H. Kang, H. Y. Park, M. Kim, J. W. Lim, D. Y. Chung, M. J. Lee, H. Choe, Y. E. Sung, *Nat. Commun.* **2013**, *4*, 2473.
- [127] J. Kibsgaard, A. Jackson, T. F. Jaramillo, *Nano Energy* **2016**, *29*, 243.
- [128] J. Kibsgaard, Y. Gorlin, Z. Chen, T. F. Jaramillo, *J. Am. Chem. Soc.* **2012**, *134*, 7758.
- [129] T. Tamaki, H. Kuroki, S. Ogura, T. Fuchigami, Y. Kitamoto, T. Yamaguchi, *Energy Environ. Sci.* **2015**, *8*, 3545.
- [130] T. Chen, S. Liu, J. Zhang, M. Tang, *Int. J. Heat Mass Transfer* **2019**, *128*, 1168.
- [131] J. H. Chun, K. T. Park, D. H. Jo, S. G. Kim, S. H. Kim, *Int. J. Hydrogen Energy* **2011**, *36*, 1837.
- [132] S. Flick, M. Schwager, E. McCarthy, W. Mérida, *Appl. Energy* **2014**, *129*, 135.
- [133] L. Cindrella, A. M. Kannan, J. Lin, K. Saminathan, Y. Ho, C. Lin, J. Wertz, *J. Power Sources* **2009**, *194*, 146.
- [134] W.-M. Yan, C.-Y. Hsueh, C.-Y. Soong, F. Chen, C.-H. Cheng, S.-C. Mei, *Int. J. Hydrogen Energy* **2007**, *32*, 4452.
- [135] H. Oh, J. Park, K. Min, E. Lee, J.-Y. Jyoung, *Appl. Energy* **2015**, *149*, 186.
- [136] P. Shrestha, D. Ouellette, J. Lee, N. Ge, A. K. C. Wong, D. Muirhead, H. Liu, R. Banerjee, A. Bazylak, *Adv. Mater. Interfaces* **2019**, *6*, 1901157.
- [137] D. Ko, S. Doh, H. S. Park, M. H. Kim, *Int. J. Hydrogen Energy* **2018**, *43*, 2369.
- [138] M. Balakrishnan, P. Shrestha, N. Ge, C. Lee, K. F. Fahy, R. Zeis, V. P. Schulz, B. D. Hatton, A. Bazylak, *ACS Appl. Energy Mater.* **2020**, *3*, 2695.
- [139] D. Gerteisen, T. Heilmann, C. Ziegler, *J. Power Sources* **2008**, *177*, 348.
- [140] X. Wang, S. Chen, Z. Fan, W. Li, S. Wang, X. Li, Y. Zhao, T. Zhu, X. Xie, *Int. J. Hydrogen Energy* **2017**, *42*, 29995.
- [141] A. Forner-Cuenca, J. Biesdorf, A. Lamibrac, V. Manzi-Orezzoli, F. Büchi, L. Gubler, T. J. Schmidt, P. Boillat, *J. Electrochem. Soc.* **2016**, *163*, F1038.
- [142] A. Forner-Cuenca, J. Biesdorf, V. Manzi-Orezzoli, L. Gubler, T. J. Schmidt, P. Boillat, *J. Electrochem. Soc.* **2016**, *163*, F1389.
- [143] G. Wang, Y. Utaka, S. Wang, *Energies* **2020**, *13*, 3529.
- [144] T. G. Tranter, P. Boillat, A. Mularczyk, V. Manzi-Orezzoli, P. Shearing, D. Brett, J. Eller, J. Gostick, A. Forner-Cuenca, *J. Electrochem. Soc.* **2020**, *167*, 114512.
- [145] J. Park, H. Oh, Y. I. Lee, K. Min, E. Lee, J.-Y. Jyoung, *Appl. Energy* **2016**, *171*, 200.
- [146] T. Li, K. Wang, J. Wang, Y. Liu, Y. Han, J. Song, H. Hu, G. Lin, Y. Liu, *J. Mater. Sci.* **2020**, *55*, 4558.
- [147] Z. Song, Y. N. Zhu, H. Liu, M. N. Banis, L. Zhang, J. Li, K. Doyle-Davis, R. Li, T. K. Sham, L. Yang, *Small* **2020**, *16*, 2003096.
- [148] Z. Lu, J. Waldecker, X. Xie, M.-C. Lai, D. S. Hussey, D. L. Jacobson, *ECS Trans.* **2013**, *58*, 315.
- [149] J. Wei, F. Ning, C. Bai, T. Zhang, G. Lu, H. Wang, Y. Li, Y. Shen, X. Fu, Q. Li, *J. Mater. Chem. A* **2020**, *8*, 5986.
- [150] A. Forner-Cuenca, V. Manzi-Orezzoli, J. Biesdorf, M. El Kazzi, D. Streich, L. Gubler, T. J. Schmidt, P. Boillat, *J. Electrochem. Soc.* **2016**, *163*, F788.
- [151] X. Li, I. Sabir, *Int. J. Hydrogen Energy* **2005**, *30*, 359.
- [152] A. Manso, F. Marzo, J. Barranco, X. Garikano, M. G. Mujika, *Int. J. Hydrogen Energy* **2012**, *37*, 15256.
- [153] T. D. Tran, S. Huang, D. H. Vu, V. N. Duy, *Int. J. Electrochem. Sci.* **2018**, *13*, 10480.
- [154] J. P. Kloess, X. Wang, J. Liu, Z. Shi, L. Guessous, *J. Power Sources* **2009**, *188*, 132.
- [155] G. Cai, Y. Liang, Z. Liu, W. Liu, *Energy* **2020**, *192*, 116670.
- [156] G. W. Lee, G. H. Shim, J. M. Kim, C. Seol, J. H. Kim, S. M. Kim, H. S. Ahn, *Int. J. Hydrogen Energy* **2020**, *45*, 12972.
- [157] G. W. Lee, C. Seol, K. M. Kim, S. T. Lim, G. H. Shim, S. M. Kim, H. S. Ahn, *Int. J. Hydrogen Energy* **2021**, *46*, 36930.
- [158] S. Jang, H.-Y. Park, J. Jung, J. Lee, H.-Y. Park, J. H. Jang, S. M. Kim, S. J. Yoo, *ACS Sustainable Chem. Eng.* **2019**, *7*, 15487.
- [159] W. Yuan, Y. Tang, X. Yang, Z. Wan, *Appl. Energy* **2012**, *94*, 309.

- [160] J. E. Park, J. Lim, S. Kim, I. Choi, C.-Y. Ahn, W. Hwang, M. S. Lim, Y.-H. Cho, Y.-E. Sung, *Electrochim. Acta* **2018**, 265, 488.
- [161] J. Kim, N. Cunningham, *J. Power Sources* **2010**, 195, 2291.
- [162] S. Huo, N. J. Cooper, T. L. Smith, J. W. Park, K. Jiao, *Appl. Energy* **2017**, 203, 101.
- [163] T. Yoshida, K. Kojima, *Electrochem. Soc. Interface* **2015**, 24, 45.
- [164] Y. Nonobe, *IEEJ Trans. Electr. Electron. Eng.* **2017**, 12, 5.
- [165] J. Kim, G. Luo, C.-Y. Wang, *J. Power Sources* **2017**, 365, 419.
- [166] J. Kim, G. Luo, C.-Y. Wang, *J. Power Sources* **2018**, 400, 284.
- [167] G. Zhang, B. Xie, Z. Bao, Z. Niu, K. Jiao, *Int. J. Energy Res.* **2018**, 42, 4697.
- [168] S. Pedram, M. Batool, K. Yapp, L. Bonville, J. Jankovic, *Adv. Energy Sustainability Res.* **2021**, 2, 2000092.
- [169] C.-J. Tseng, B. T. Tsai, Z.-S. Liu, T.-C. Cheng, W.-C. Chang, S.-K. Lo, *Energy Convers. Manage.* **2012**, 62, 14.
- [170] D. K. Shin, J. H. Yoo, D. G. Kang, M. S. Kim, *Renewable Energy* **2018**, 115, 663.
- [171] A. El-Kharouf, T. J. Mason, D. J. Brett, B. G. Pollet, *J. Power Sources* **2012**, 218, 393.
- [172] H. Lee, H. Kim, H. Kim, *J. Electrochem. Soc.* **2019**, 166, F74.
- [173] Y. Sim, J. Kwak, S.-Y. Kim, Y. Jo, S. Kim, S. Y. Kim, J. H. Kim, C.-S. Lee, J. H. Jo, S.-Y. Kwon, *J. Mater. Chem. A* **2018**, 6, 1504.
- [174] J. Shen, Z. Tu, S. H. Chan, *Appl. Therm. Eng.* **2020**, 164, 114464.
- [175] W. Huang, B. Yang, Y. Zhao, Z. Ding, *J. Mater. Chem.* **2010**, 20, 3367.
- [176] J. Hu, H. Meng, G. Li, S. I. Ibekwe, *Smart Mater. Struct.* **2012**, 21, 053001.
- [177] H. Koerner, G. Price, N. A. Pearce, M. Alexander, R. A. Vaia, *Nat. Mater.* **2004**, 3, 115.
- [178] J. K. Kim, S. I. Cho, N. G. Kim, M. S. Jhon, K. S. Min, C. K. Kim, G. Y. Yeom, *J. Vac. Sci. Technol., A* **2013**, 31, 021301.
- [179] K. A. Pears, J. Stolze, *Microelectron. Eng.* **2005**, 81, 7.
- [180] K. Takahata, Y. B. Gianchandani, *J. Microelectromech. Syst.* **2002**, 11, 102.
- [181] Z. Xiao, M. Dahmardeh, M. V. Moghaddam, A. Nojeh, K. Takahata, *Microelectron. Eng.* **2016**, 150, 64.
- [182] S. Mooraj, Z. Qi, C. Zhu, J. Ren, S. Peng, L. Liu, S. Zhang, S. Feng, F. Kong, Y. Liu, *Nano Res.* **2021**, 14, 2105.
- [183] B. Gadagi, R. Lekurwale, *Mater. Today: Proc.* **2021**, 45, 277.
- [184] C. Xu, A. Bouchemit, G. L'Espérance, L. L. Lebel, D. Therriault, *J. Mater. Chem. C* **2017**, 5, 10448.
- [185] R. Yeetsorn, M. W. Fowler, C. Tzoganakis, *Nanocomposites with Unique Properties and Applications in Medicine and Industry* **2011**, 317.
- [186] S. T. Thompson, B. D. James, J. M. Huya-Kouadio, C. Houchins, D. A. DeSantis, R. Ahluwalia, A. R. Wilson, G. Kleen, D. Papageorgopoulos, *J. Power Sources* **2018**, 399, 304.
- [187] A. Willert, F. Z. Tabary, T. Zubkova, P. E. Santangelo, M. Romagnoli, R. R. Baumann, *Int. J. Hydrogen Energy* **2022**, 47, 20973.
- [188] M. Stähler, A. Stähler, F. Scheepers, M. Carmo, D. Stolten, *Int. J. Hydrogen Energy* **2019**, 44, 7053.
- [189] J. E. Park, W. Hwang, M. S. Lim, S. Kim, C.-Y. Ahn, O.-H. Kim, J.-G. Shim, D. W. Lee, J. H. Lee, Y.-H. Cho, *Int. J. Hydrog. Energy* **2019**, 44, 22074.
- [190] Y. Wang, T. Liu, W. He, S. Wang, S. Liu, L. Yue, H. Li, *Energy Convers. Manage.* **2020**, 223, 113297.



Segeun Jang received his Ph.D. degree from the School of Mechanical and Aerospace Engineering at Seoul National University in 2018. After, he worked at Korea Institute of Science and Technology and Hanbat National University as a postdoctoral researcher and assistant professor, respectively. Currently, he is an assistant professor in the School of Mechanical Engineering at Kookmin University in South Korea since 2021. His research has been focused on developing diverse interface engineering strategies for improving the performance of energy devices, including polymer electrolyte membrane fuel cells.



Yun Sik Kang obtained his Ph.D. degree from School of Chemical and Biological Engineering at Seoul National University in 2015 and worked with Dr. Sung Jong Yoo as a postdoctoral researcher at Korea Institute of Science and Technology. After completing his postdoctoral course, he worked as a principal research engineer at Hyundai Mobis with Dr. Sungchul Lee. Currently, he is working as a senior researcher at Korea Institute of Energy Research. His research interests include the synthesis of electrocatalysts and the development of membrane electrode assembly for fuel cells.



Sungchul Lee obtained his Ph.D. degree from Department of Chemical Engineering at Kyunghee University in 2005 and worked at Samsung SDI and Yale University as a principal research engineer and associate research scientist, respectively. Currently, he is working as a team leader in the MEA developing team at Hyundai Mobis since 2016. His research interests include the fabrication, degradation mechanism, and the scale-up study of membrane electrode assembly for polymer electrolyte membrane fuel cells.



Sang Moon Kim is currently an associate professor in the Department of Mechanical Engineering at Incheon National University in South Korea since 2016. He received his Ph.D. degree from the School of Mechanical and Aerospace Engineering at Seoul National University in 2015. He also worked at Global Frontier Center for Multiscale Energy System as a postdoctoral researcher. His research interests include multiscale design and fabrication of membrane and electrode architectures for fuel cell and filtering systems.



Sung Jong Yoo obtained his Ph.D. degree from the School of Chemical and Biological Engineering at Seoul National University in 2009 and moved to KIST for postdoctoral research, synthesizing a wide variety of advanced compounds and materials, ranging from alloys, core–shells, and hollow nanoparticles. He began his independent career in 2012 as senior research scientist in the Fuel Cell Research Center at KIST. He is currently a principal scientist at KIST. His current research interests include: 1) the multiscale-architected functional membranes and electrodes for fuel cells, and 2) the design principles for ORR or HOR activity and stability on catalysts.